Biomaterials Advances 158 (2024) 213759

Contents lists available at ScienceDirect

Biomaterials Advances

journal homepage: www.journals.elsevier.com/materials-science-and-engineering-c

Magnetically navigated microbubbles coated with albumin/polyarginine and superparamagnetic iron oxide nanoparticles

Olga I. Gusliakova [a,b,*,1], Maxim A. Kurochkin [c,1], Roman A. Barmin [c,1], Ekaterina S. Prikhozhdenko [a], Tatyana M. Estifeeva [c], Polina G. Rudakovskaya [c], Olga A. Sindeeva [b], Victor V. Galushka [d], Evgeny S. Vavaev [e], Aleksei S. Komlev [e], Evgeny V. Lyubin [e], Andrey A. Fedyanin [e], Krishna Kanti Dey [f], Dmitry A. Gorin [c,**]

[a] Science Medical Center, Saratov State University, Saratov 410012, Russia
[b] Vladimir Zelman Center for Neurobiology and Brain Rehabilitation, Skolkovo Institute of Science and Technology, Moscow 121205, Russia
[c] Center for Photonic Science and Engineering, Skolkovo Institute of Science and Technology, Moscow 121205, Russia
[d] Education and Research Institute of Nanostructures and Biosystems, Saratov State University, Saratov 410012, Russia
[e] Faculty of Physics, Lomonosov Moscow State University, Moscow 119991, Russia
[f] Department of Physics, Indian Institute of Technology Gandhinagar, Palaj, Gujarat 382055, India

ARTICLE INFO

Keywords:
Microbubbles
Ultrasound
Magnetic navigation
Magnetic tweezers
SPION
Bovine serum albumin
Poly-L-arginine
Protein–polymer complex
Drug delivery

ABSTRACT

While microbubbles (MB) are routinely used for ultrasound (US) imaging, magnetic MB are increasingly explored as they can be guided to specific sites of interest by applied magnetic field gradient. This requires the MB shell composition tuning to prolong MB stability and provide functionalization capabilities with magnetic nanoparticles. Hence, we developed air-filled MB stabilized by a protein–polymer complex of bovine serum albumin (BSA) and poly-L-arginine (pArg) of different molecular weights, showing that pArg of moderate molecular weight distribution (15–70 kDa) enabled MB with greater stability and acoustic response while preserving MB narrow diameters and the relative viability of THP-1 cells after 48 h of incubation. After MB functionalization with superparamagnetic iron oxide nanoparticles (SPION), magnetic moment values provided by single MB confirmed the sufficient SPION deposition onto BSA + pArg MB shells. During MB magnetic navigation in a blood vessel mimicking phantom with magnetic tweezers and in a Petri dish with adherent mouse renal carcinoma cell line, we demonstrated the effectiveness of magnetic MB localization in the desired area by magnetic field gradient. Magnetic MB co-localization with cells was further exploited for effective doxorubicin delivery with drug-loaded MB. Taken together, these findings open new avenues in control over albumin MB properties and magnetic navigation of SPION-loaded MB, which can envisage their applications in diagnostic and therapeutic needs.

1. Introduction

Ultrasound (US) imaging is routinely used in the clinic, ensuring the procedure advantages of non–invasiveness, low cost, and absence of ionizing radiation [1]. However, the contrast resolution of US is limited, which may hinder its use in the diagnosis of certain pathologies [2], and can be improved by the administration of echogenic contrast agents, *i.e.* microbubbles (MB) [3,4]. MB are gas–filled vesicles with a diameter of 1–7 μm, stabilized by nano–sized shells composed of lipids, proteins, or polymers [5]. The choice of the shell materials primarily determines the acoustic response of the synthesized MB, as well as their functionalization capabilities [6]. For instance, soft lipid shells offer a superior acoustic profile in terms of MB echogenicity, but have finite stability and limited additive loading capabilities [7]. In contrast, rigid polymer MB shells possess long shelf–life stability and high loading capabilities, while acoustic response is diminished [8]. MB with soft protein shells act as a compromise between lipid and polymeric MB counterparts, yet require improvements in their colloidal stability and acoustic profile [9].

* Correspondence to: O.I. Gusliakova, Science Medical Center, Saratov State University, Saratov 410012, Russia.
** Corresponding author.
E-mail addresses: olga.gusliakova17@gmail.com (O.I. Gusliakova), d.gorin@skoltech.ru (D.A. Gorin).
[1] These authors contributed equally to this work.

https://doi.org/10.1016/j.bioadv.2024.213759
Received 22 September 2023; Received in revised form 31 December 2023; Accepted 1 January 2024
Available online 9 January 2024
2772-9508/© 2024 Elsevier B.V. All rights reserved.

By tuning the composition of MB, the acoustic performance and functionalization capabilities of MB can be enriched [10–12]. Recently, the concept of "hybrid MB shell" has been proposed, combining both soft (lipid or protein) and rigid (polymer) shell materials to balance the properties of a single MB composition [13–15]. Thereby, we considered bovine serum albumin (BSA) since BSA shares the same molecular weight (66.5 kDa), preserved disulfide bonds pattern, and 76 % structural identity with human serum albumin, with a 5–7-fold reduction in cost [16]. Poly–L–arginine (pArg) polymer is a poly(amino acid) that has a long record of use in the design of biomaterials to improve their biocompatibility [17–19]. The presence of a large number of amine groups, which determine the positive charge of pArg chains [20], suggests intense interactions with the negatively charged BSA globules [21], which may improve the MB stability.

In recent years, functional MB have been increasingly explored, combining the US stimuli–responsiveness of the MB template with additional functional capabilities prescribed by additives [22]. Magnetic MB, which can be manipulated by both acoustic and magnetic fields, are of particular interest because they can be delivered to the region of interest by magnetic field [23], and combined magnetic resonance imaging/therapeutic US devices have recently been approved for clinical use [24]. Previous reports have focused on MB functionalization routes with superparamagnetic iron oxide nanoparticles (SPION) [25,26] or preclinical evaluation of magnetic MB applications, including sonopermeation monitoring [27], bimodal molecular imaging [28], and magnetically targeted drug delivery [29,30]. However, *in vitro* studies on direct magnetic manipulation of MB can bridge the gap between ongoing research in functional MB formulations and their preclinical evaluation.

In this study, we developed SPION-functionalized MB with hybrid BSA + pArg shell for *in vitro* magnetic navigation. We identified the MB optimal composition based on BSA + pArg complex, showing that pArg of moderate molecular weight distribution [15–70 kDa] provided MB with enhanced shell stability, significant *in vitro* and *in vivo* acoustic response, and did not provide cytotoxicity after 48 h of incubation with THP-1 cells. Once BSA + pArg MB were functionalized with SPION, we showed the controlled magnetic navigation using a blood vessel mimicking phantom with magnetic tweezers and co-incubation with RenCa adherent cell culture under external magnetic field. When MB shells were loaded with doxorubicin, magnetic co-localization of MB and RenCa cells promoted significant cytotoxic effect on cells 48 and 72 h after treatment initiation, while MB alone did not show any cytotoxicity. These findings demonstrate the benefits of tuning MB shell properties through the protein–polymer complex incorporation and magnetic navigation of SPION-loaded MB, which can envisage their (bio)applications that require applied magnetic and acoustic fields.

2. Materials and methods

2.1. Materials

Reagent	Source	Identifier
Bovine serum albumin (BSA)	Sigma Aldrich	CAS # 9048–46–8 Product # A2153
Poly–L–arginine with molecular weight 5–15 kDa (pArg [5–15 kDa])	Sigma Aldrich	CAS # 26982–20–7 Product # P4663
Poly–L–arginine with molecular weight 15–70 kDa (pArg [15–70 kDa])	Sigma Aldrich	CAS # 26982–20–7 Product # P7762
Poly–L–arginine with molecular weight > 70 kDa (pArg [>70 kDa])	Sigma Aldrich	CAS # 26982–20–7 Product # P3892
Bradford Reagent	Sigma Aldrich	Product # B6916
Rhodamine B isothiocyanate (RITC)	Sigma Aldrich	CAS # 36877–69–7 Product # R1755
Fluorescein 5(6) isothiocyanate (FITC)	Sigma Aldrich	CAS # 27072–45–3 Product # F3651
Tetramethylrhodamine isothiocyanate (TRITC)	Sigma Aldrich	CAS # 95197–95–8 Product # 87918
Superparamagnetic iron oxide nanoparticles (SPION) with citric acid coating, and hydrodynamic diameter of 10 ± 3 nm	TetraQuant Ltd.	N/A
Sodium chloride (NaCl)	Sigma Aldrich	CAS # 7647–14–5 Product # S9888
Dulbecco's Modified Eagle Medium (DMEM)	Gibco	Cat # 11965092
Roswell Park Memorial Institute medium (RPMI-1640)	Gibco	Cat # 11875093
One Shot Fetal Bovine Serum (FBS)	ThermoFisher Scientific	Cat # A3160802
2–Mercaptoethanol	ThermoFisher Scientific	Cat # 125472500
Penicillin–Streptomycin (10,000 U/mL)	ThermoFisher Scientific	Cat # 15140122
AlamarBlue™ Cell Viability Reagent	Invitrogen	Cat # DAL1100
Hanks' Balanced Salt Solution (HBSS)	ThermoFisher Scientific	Cat # 14175095
Calcein AM solution	Sigma Aldrich	CAS # 148504–34–1 Product # C1359
Hoechst 33258	Invitrogen	Cat # H3569
Doxorubicin hydrochloride (Dox)	Sigma Aldrich	CAS # 25316–40-9
N-(3-Dimethylaminopropyl)-N′-ethylcarbodiimide hydrochloride (EDC)	Sigma Aldrich	CAS # 25952–53-8
N-Hydroxysuccinimide (NHS)	Sigma Aldrich	CAS # 6066-82-6
Propidium Iodide (PI)–1.0 mg/mL Solution in Water	ThermoFisher Scientific	Cat # P3566

Deionized (DI) water produced with a MilliQ water treatment system (Merck Millipore, Germany) was used in all experimental stages.

2.2. Methods

2.2.1. BSA and pArg conjugation with fluorescent dyes (BSA–RITC, BSA–FITC, pArg–TRITC)

BSA–RITC and BSA–FITC: BSA was labeled with RITC or FITC similar to the method described previously [31]. Briefly, BSA (160 mg) was dissolved in PBS buffer (0.1 M, 40 mL, pH 8.3). RITC or FITC (25 mg) were dissolved in ethanol (5 mL). BSA and RITC or BSA and FITC solutions were mixed under gentle stirring for 12 h in dark and 4 °C. Next, freshly prepared BSA–RITC or BSA–FITC solutions were dialyzed for 3 days in DI water. Finally, BSA labeled with RITC or FITC was freeze–dried and stored at −20 °C.

pArg–TRITC: pArg [15–70 kDa] (10 mg) was dissolved in PBS buffer (0.01 M, 50 mL, pH 7.8). TRITC (5 mg) was dissolved in DMSO (5 mL). Solutions were mixed under gentle stirring for 12 h in dark and 4 °C. Next, solution was dialyzed for 3 days in DI water and filtered. Finally, pArg–TRITC was freeze–dried and stored at −20 °C.

2.2.2. BSA conjugation with doxorubicin hydrochloride (BSA–Dox)

BSA (100 mg) was dissolved in DI water (7 mL). Dox (3 mg), NHS (2.7 mg), and EDC (9.9 mg) were dissolved in DI water (each in 1 mL). All solutions were mixed together with gentle stirring for 45 min in the dark. Next, freshly prepared BSA–Dox solutions were dialyzed for 3 days in saline. Finally, BSA–Dox was freeze–dried and stored at −20 °C.

2.2.3. BSA and pArg complexation study (turbidimetry and dynamic light scattering measurements)

Solutions of BSA (400 μL, 100 mg/mL) and pArg with selected molecular weight distributions (400 μL, 1 mg/mL) were mixed in an Eppendorf tube and placed in the water bath under moderate heating (55 °C). 50 μL of the mixture was taken before and 1, 5, 10, 15, and 60 min after the start of the heating. 950 μL of physiological saline was added to each aliquot. 200 μL of the diluted aliquot was used for absorbance spectral analysis on a Synergy H1 microplate reader (BioTek Instruments, Inc., USA) and 750 μL was used for size distribution analysis with dynamic light scattering (DLS) measurements on a Zetasizer Nano ZS analyzer (Malvern Panalytical, UK).

2.2.4. MB synthesis and functionalization with SPION

MB with the shell of BSA–pArg complex were synthesized similar to our previous reports [32]. Briefly, a mixture of BSA (100 mg/mL, 1 mL) and pArg of specified molecular weight distribution (1 mg/mL, 1 mL) solutions was placed in a glass vial, preheated in a water bath at 55 °C for 15 min and subsequently sonicated for 3 min at 100 W (Sonopuls HD 2070 equipped with MS 73 sonotrode, Bandelin Electronic GmbH & Co KG, Germany). After MB synthesis, MB were left overnight in a refrigerator (+4 °C) to allow MB to float to the air–liquid interface of a vial, forming a "MB cake". The liquid phase was then carefully removed, 1 mL of physiological saline was added, and the MB cake was slowly redispersed. The washing procedure was repeated until the saline solution under the MB cake was clear.

For functionalization with SPION, 1 mL of uniformly dispersed BSA + pArg MB was mixed with a 1 mL of SPION suspension, keeping the ionic strength of the mixture equal to the physiological saline to prevent aggregation. The resulting MB and SPION mixture was gently stirred and left overnight in a refrigerator (+4 °C). Next, washing was performed as for plain MB until the solution under the MB cake was clear. The composition of resulting magnetic MB was 5 mg of BSA, 50 μg of pArg and 0.4 mg of SPION.

To confirm the uniform distribution of BSA and pArg in MB shells, 2 mg of BSA–FITC and 0.2 mg of pArg–TRITC were added to unstained BSA and pArg prior to MB synthesis. To perform microscopy with cell cultures, 2 mg of BSA–RITC was added to unstained BSA prior to MB synthesis. For study of RITC fluorescence quenching after SPION adsorption, lyophilized BSA–RITC of various weights (0.4, 1.0, 2.0, and 4.0 mg) were added to unstained BSA prior to MB synthesis. To study the interaction between MB and cells, 1 mL of BSA–RITC (1 mg/mL) or BSA–Dox (10 mg/mL) were added to intact BSA prior to MB synthesis. Further manipulations were performed according to procedures described above.

2.2.5. Microscopy characterization

Confocal laser scanning microscopy (CLSM) was carried out on an Axio Observer.Z1/7 with a Plan–Apochromat 40×/1.3Oil DIC (UV) VIS–NIR M27 objective (Carl Zeiss Microscopy GmbH, Germany) to evaluate the distribution of BSA and pArg in the MB shell, and on a CLSM Leica TCS SP8 X (Leica Biosystems GmbH, Germany) using a Secure–Seal™ Spacer (8 wells, 9 mm diameter, 0.12 mm deep, ThermoFisher Scientific) to conduct *in vitro* experiments, as well as imaging of BSA–RITC labeled MB before and after SPION adsorption. 405 nm, 488 nm, 514 nm or 532 nm lasers were used for imaging of THP–1 and RenCa cells incubated with MB containing BSA–RITC or BSA–Dox. The detection ranges were set as follows: 415–475 nm, 500–550 nm, 570–700 nm, 590–650 nm to image nuclei, cytoplasm and MB or PI, respectively. To record images, a sequence scan was performed, in which each channel was irradiated and detected sequentially. Three–dimensional scans were performed to determine the localization of MB in experiments using a magnet. The z–stack height was 320 μm. The imaging parameters of MB containing BSA–RITC before and after SPION adsorption were as follows: 514 nm laser and 550–650 detection range. The lambda scan was performed in the range of 530–700 nm in 30 steps with a detection width of 20 nm.

Scanning electron microscopy (SEM) was performed with a MIRA II LMU instrument (Tescan, Czech Republic) at an operating voltage of 30 kV. Prior to measurements, 5 μL drops from the purified MB samples were dried on silicon substrates and then sputtered with gold. The MB diameter distribution was calculated using the free ImageJ software (National Institutes of Health, USA) by measuring the diameter of 100 MB for each sample.

Transmission electron cryomicroscopy (CryoTEM) analysis was performed with Tecnai G212 instrument (SPIRIT FEI, USA) in liquid N2. Prior to measurements, 3 μL of the sample was applied to a 200 mesh copper grid pre–treated with plasma and covered with lacey film. Excess sample was removed by blotting the grid for 1 s and immediately immersed in liquid ethane (automated immersion system, Vitrobot FEI, USA).

2.2.6. US imaging in phantoms

MB were tested for echogenicity using the DUB Skinscanner device (Taberna Pro Medicum GmbH, Germany) equipped with Doppler transducer with the frequency of 22 MHz and mechanical index of 0.16. To mimic *in vivo* vessel conditions, polyethylene tubes were filled with MB samples or physiological saline used as a control, sealed on both sides with Parafilm and embedded in the US gel prior to B-mode US imaging. Calculation of the observed echogenicity was performed using the ImageJ software (National Institutes of Health, USA) by estimating the mean gray signal intensity value (corresponding to the B–mode US signal) in uniform ROIs at 3 different image locations for each sample. The final intensity value is presented as the mean ± standard deviation of three samples. Statistical significance was evaluated by one–way ANOVA test using GraphPad Prism 6 software.

2.2.7. Cytotoxicity assay

The human monocyte suspension (THP-1) cell line was used for the cytotoxicity study. THP-1 was cultured in RPMI–1640 medium supplemented with a 10 % FBS, 0.05 mM 2–mercaptoethanol, and 1 % penicillin/streptomycin. The relative metabolic activity of THP–1 cells after incubation with MB was determined by metabolic activity within reduction of the AlamarBlue reagent. Cells were seeded in 96–well plates at a density of 10×10^3 cells per well. The next day, the MB suspension was diluted 10–fold and all separate shell components (10 μg of BSA, 0.1 μg of pArg, 20 μL of saline) were added to the wells with fresh media after aspiration of the old media. For control cells group, only medium replacement was performed. The cells were incubated together with the added samples for 48 h, followed by media aspiration. Next, 90 μL of the fresh culturing media was added to each well, followed by the addition of AlamarBlue reagent (10 μL). Cells were incubated with resazurin agent for 3 h, and fluorescence intensity was measured at excitation/emission wavelengths of 560/590 nm using a Synergy H1 microplate reader (BioTek Instruments, Inc., USA).

The mouse renal carcinoma (RenCa) cell line was used in a comparative cytotoxicity study with implemented magnetic co-localization of MB with adherent cells. RenCa was cultured in RPMI–1640 medium supplemented with a 10 % FBS, and 1 % penicillin/streptomycin. The relative metabolic activity of RenCa cells after incubation with MB in the absence and presence of a magnetic field gradient was measured using AlamarBlue reagent. Cells were seeded in 96–well plates at a density of 5×10^3 cells per well. The next day, the MB loaded with BSA–Dox and SPION (10 nM of Dox per well) were added to the wells with fresh media after aspiration of the old media. For control cells

group, only medium replacement was performed. Nine wells were placed on an external magnetic field source and left for 30 min after the addition of MB–containing media. Another nine wells were left without the exposure to a magnetic field gradient. After 30 min, 70 % of the culture medium was carefully aspirated from the top and replaced with fresh medium. Further cell incubation was carried out at 37 °C and in an atmosphere containing 5 % CO_2. Every 24 h (24 h, 48 h, 72 h), the media was aspirated and replaced with 90 μL of the fresh media, followed by the addition of AlamarBlue reagent (10 μL). Cells were incubated with resazurin agent for 4 h, and fluorescence intensity was measured at excitation/emission wavelengths of 560/590 nm using a Synergy H1 microplate reader (BioTek Instruments, Inc., USA). After the measurements, the medium was renewed in each well and the cells were left for further incubation. The 72–hour time point was the terminal time point.

Relative metabolic activity was calculated as the ratio of the mean value of the relative fluorescent units of the experimental group to the mean value of the control group, expressed as a percentage.

2.2.8. *In vivo US imaging*

The laboratory animals were treated according to the rules of Saratov State Medical University (Ethics Committee Protocol No. 8, dated 7th of March 2023) and the Geneva Convention of 1985 (International Guiding Principles for Biomedical Research Involving Animals). All experimental procedures were performed on the Wistar rat (230–250 g weight) using general anesthesia (Zoletil mixture (30 mg/kg, 75 μL, Virbac SA, France) and Ksila (20 mg/kg, 25 μL, Interchemie Werken 'de Adelaar' BV, the Netherlands)) *via* intraperitoneal injection. At the end of the experiment, the animals were euthanized by an overdose of anesthesia.

Briefly, 200 μL of MB suspension in saline was administered intravenously (*via* the tail or jugular vein) for US imaging of the large vessels and the heart. An insulin syringe with a 27 G needle was used for tail vein injection, while a butterfly catheter was used for jugular vein injection. *In vivo* US images were recorded using the same DUB Skin-scanner setup used for *in vitro* US imaging.

2.2.9. *Assessment of RITC fluorescence quenching degree in MB after SPION adsorption*

To assess the degree of quenching of RITC fluorescence in MB after SPION adsorption, a lambda scan was recorded on a CLSM. The excitation wavelength was fixed (514 nm) and a series of images with narrow detection ranges were taken (image size 1024 × 1024 px; detection width per image, 20 nm; total detection range, 550–650 nm; number of recorded images per sample, 30). Next, square areas of 200 × 200 px in size were cropped from the lambda scan, and a fluorescence graph was plotted from the average pixel intensity. This resulted in 25 fluorescence spectra obtained from the lambda scan.

Lambda scans were recorded for eight samples: MB were produced with four concentrations of the BSA–RITC conjugate (0.4, 1.0, 2.0, and 4.0 mg per synthesis) in the presence or absence of SPION in MB shells. Since the MB concentration decreased with the incorporation of SPION, the intensity of the obtained spectra was additionally normalized by the percentage of the image area filled with MB, calculated using the mask according to the Otsu method in the Gwyddion software (Czech Metrology Institute, Czech Republic) [33]. The final fluorescence quenching coefficient was estimated as the difference between the concentration normalized fluorescence intensity of MB without SPION (taken as 100 %) and with SPION embedded in the shells.

2.2.10. *Magnetic moment and magnetic polarizability measurements with optical tweezers*

Measurements of MB magnetic properties with optical tweezers were performed according to the method described in [34], and details of the experimental setup are similar to ones reported in [35,36]. Briefly, 45 μL of MB suspension was placed in a sealed cell consisting of two coverslips separated by a layer of adhesive tape and soft paraffin. In the sample area, two optical traps of the experimental setup were created using tightly focused radiation from two single–mode lasers with a wavelength of 980 nm and an optical power adjustable from 0 to 330 mW. A system of four electromagnets was placed around the sample to apply an external magnetic field. The MB trajectories were recorded using quadrant photodiodes, registering the radiation of two additional lasers scattered by MB. A comprehensive analysis of the thermal motion of trapped MB and the correlated motion of a pair of interacting MB in an external alternating magnetic field made it possible to determine the magnetic characteristics of the single MB. The detailed procedure is described in Section S1 of Supporting information.

2.2.11. *MB magnetic entrapment with magnetic tweezers*

Magnetic entrapment of MB was performed with the homemade electromagnetic tweezers consisting of two separate electromagnets with concentrators connected by a steel contactor of the same material and sharpened at one end. The distance between the sharpened ends of the concentrators was adjusted with micron accuracy using the precision rotary stage. The tweezers were mounted on a base to allow us to adjust their position in a controllable manner. The magnetic field in the gap between the magnetic tweezer tips was measured using a TM-197 magnetic field meter (Tenmars Electronics, Taiwan). The gap between the magnetic tweezer tips was adjusted to 3 mm in all experiments.

The capillary phantom had a square cross–sectional shape with an internal channel size of 2680 × 200 μm. The capillary was pre–treated with heparin to prevent the MB from adhering to the inner wall of the channel and was located in the gap between the sharp tips of the tweezers. The MB suspension was pumped through the channel with a syringe pump at an average flow rate of 4.5 mL/min. The tweezers were activated 1 min after the channel was filled with the MB suspension.

An inverted optical microscope was used to image MB, and the configuration is described in [37]. A series of gray-scale images were recorded at a frame rate of 114 fps, an exposure time of 5 ms, and a resolution of 2048 × 1536 px. The MB flow dynamics in the phantom capillary before and after magnetic field activation was analyzed using the micro–scale Particle Image Velocimetry approach with the interrogation regions size of 30 × 30 px. In addition, the motion of isolated MB under an applied magnetic field was tracked and imaged using frame–by–frame digital image processing based on the Niblack local brightness threshold [38], with Niblack adaptive filtering applied separately for each image interrogation region size of 60 × 60 px.

2.2.12. *In vitro MB magnetic navigation in the presence of cell culture*

The mouse renal carcinoma (RenCa) cell line was used for *in vitro* MB magnetic navigation experiments. RenCa cells were cultured in RPMI-1640 supplemented with 10 % FBS and 1 % penicillin/streptomycin. RenCa cells were seeded in a Nunc™ Lab–Tek™ 4–well Chambered Coverglass at a density of 150 × 10^3 cells per well. Cells were incubated at 37 °C and 5 % CO_2 overnight. For fluorescence microscopy, cells were stained with Calcein AM and Hoechst 33258. A staining mixture was prepared in culture medium without FBS and antibiotic/antimycotic (6 mL of RPMI–1640, 2 μL of Calcein AM, 2 μL of Hoechst 33258). A staining mixture (600 μL) was added to the wells containing cells pre–washed with HBSS buffer. Dye incubation lasted for 15 min, followed by washing with HBSS. MB (20 MB per cell) were then added to the cells in two wells located at opposite ends of the Chambered Coverglass. One edge of the Chambered Coverglass was placed on a cylindrical NdFeB permanent magnet (diameter of 45 mm, height of 30 mm) for 10 min, as shown in Fig. S1a (incubation was performed at room temperature). The relation between magnetic induction and distance from the permanent NdFeB magnet of a cylindrical shape is presented in Fig. S1b, showing similar values of magnetic induction in the centre and the edge parts of the magnet. Measurements were carried out at room temperature. After the specified time, the Chambered Coverglass was immediately transferred to the CLSM Leica TCS SP8 stage and confocal images of the co–incubation of cells and MB were obtained.

Similar procedure was performed in the experiment with MB loaded

with BSA–Dox and SPION. RenCa cells were seeded at a density of 100 × 10^3 cells per chambered coverglass well. Cells were incubated overnight at 37 °C and in 5 % CO_2. Drug–loaded magnetic MB were added to the wells. One group of chambers were placed on the magnetic field gradient source for 30 min. Another group remained without magnetic field exposure. Culture media was carefully aspirated from the top and the fresh media was added. Further incubation was performed at 37 °C and in a 5 % CO_2 atmosphere. Prior to CLSM visualization (30 min, 24, 48 and 72 h after MB addition) cells were stained with Calcein AM, Hoechst 33258 and PI. A staining mixture was prepared in culture medium without FBS and antibiotic/antimycotic (6 mL of RPMI–1640, 2 μL of Calcein AM, 2 μL of Hoechst 33258, 30 μL of PI). A staining mixture (600 μL) was added to the wells containing cells prewashed with HBSS buffer. The staining incubation lasted for 15 min, followed by washing with HBSS and addition of fresh medium. Cells were visualized using a Leica TCS SP8 X.

3. Results

3.1. Synthesis of the protein–polymer complex between BSA and pArg of different molecular weight distributions

Prior to the MB synthesis, we evaluated the interaction of the BSA protein and pArg polymer with a molecular weight distribution of 5–15 kDa, 15–70 kDa, and >70 kDa (labeled as pArg [5–15 kDa], pArg [15–70 kDa], pArg [>70 kDa], respectively) to promote a stable protein–polymer complex formation.

Initially, we assessed the turbidity of the final solution after the addition of pArg to BSA, followed by mixing and heating at 55 °C (representative photographs of vials are shown in Fig. S2). The temperature was chosen as optimal for BSA pre–treatment to form MB with a stable shell [32,39]. The absorption spectra of BSA solutions were measured before and after the addition of pArg to note changes in the absorbance (referring to turbidity) of the resulting mixtures (Fig. 1a–c). The absorption band of the BSA in aqueous solution was located at a wavelength of 278 nm [40], and this band did not shift after the pArg

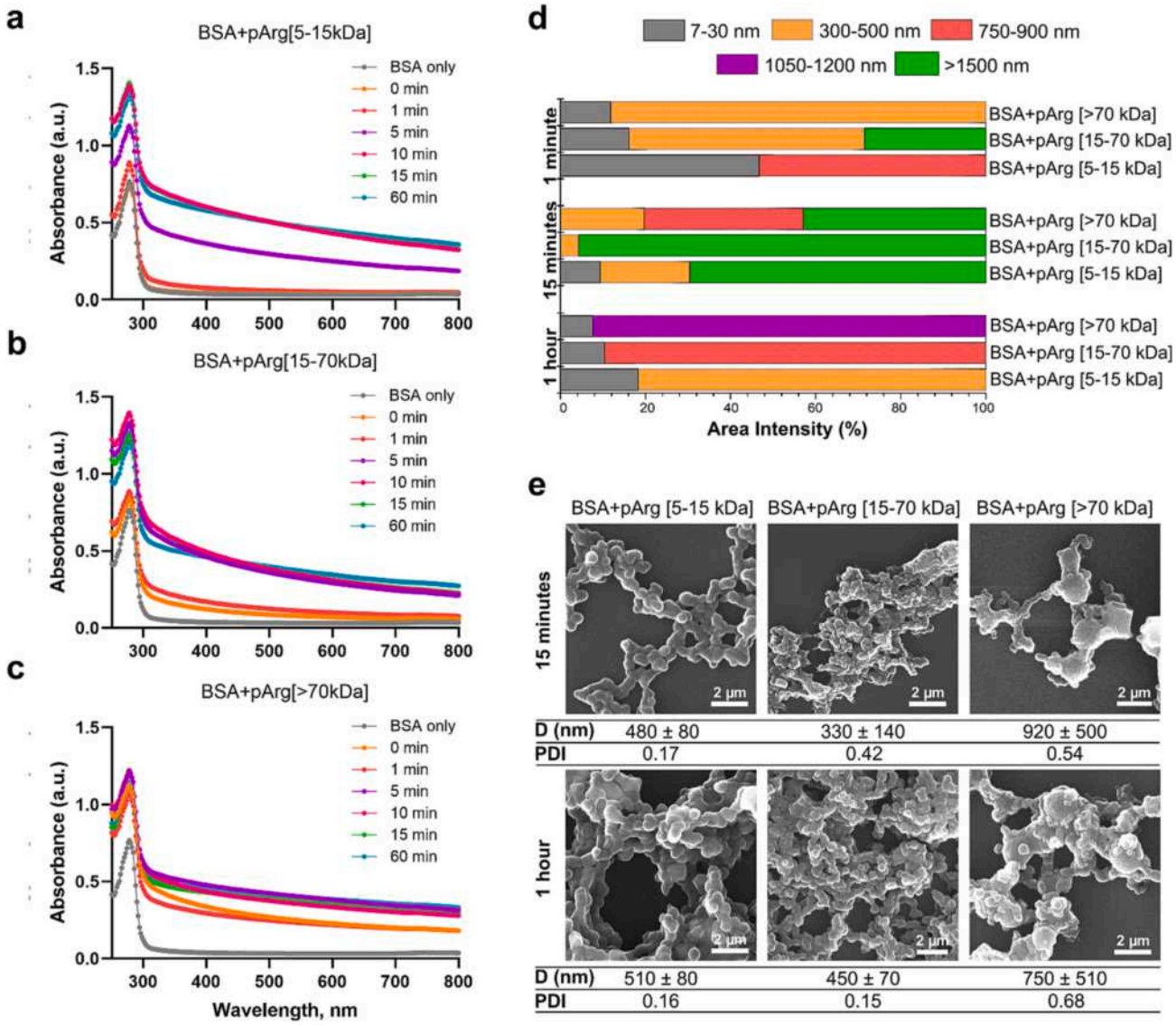

Fig. 1. BSA + pArg complex formation. Absorption spectra of solutions of the BSA + pArg complex before and after 1, 5, 10, 15, and 60 min of heating in a water bath at 55 °C for polymers with a molecular weight distributions of (a) 5–15 kDa, (b) 15–70 kDa and (c) >70 kDa (labeled as pArg [5–15 kDa], pArg [15–70 kDa], and pArg [>70 kDa], respectively). (d) The hydrodynamic diameter of BSA + pArg complex formation measured by DLS. (e) SEM images of particles formed as a result of BSA + pArg complex formation, showing their mean hydrodynamic diameter (D) ± standard deviation and polydispersity index (PDI).

introduction, but increased in its intensity. Absorption also increased in the near infra–red region, which is not typical for true BSA and pArg solutions, whose optical density tends to zero in this spectral region. Both facts indicate the formation of large–sized complexes similar to previous reports [41]. When pArg [5–15 kDa] was added, the absorbance intensity at a wavelength of 278 nm gradually increased with the time of incubation at 55 °C and reached its maximum value after 15 min (Fig. 1a), and a similar trend was also presented at a wavelength of 800 nm. For pArg [15–70 kDa], the maximum value of optical density at a wavelength of 278 nm was reached after 10 min of heating (Fig. 1b). In contrast, the addition of pArg [>70 kDa] resulted in an instantaneous achievement of maximum absorbance (Fig. 1c).

The study of the hydrodynamic diameter distribution of BSA + pArg complexes by DLS (Fig. 1d) also indicated the formation of complexes whose diameter exceeded that of intact BSA and pArg (reported to be about 7 nm [42]). However, the measurement of large aggregates by DLS is difficult due to their rapid sedimentation. SEM images of the complexes showed an increase in the number of submicron particles formed over time and an increase in the average particle diameter for pArg [5–70 kDa] and pArg [15–70 kDa] (Fig. 1e, detailed quantification is presented in Fig. S3). Contrary to the DLS results, the smallest SEM particle size of BSA + pArg corresponds to pArg [15–70 kDa], and we hypothesize that this may be due to the tendency of the resulting particles to aggregate, which made DLS measurements challenging [43]. For pArg [>70 kDa], particles of two fractions are formed: small particles (0.5 μm or less) and large particles (>1 μm), leading to high PDI values for this sample. Overall, the results indicate the complexation between BSA and pArg during the heating to 55 °C.

For further use of the BSA + pArg complex as a shell stabilizer in the MB synthesis, an optimal heating time of 15 min was chosen because the absorbance values (refer to turbidity) for all solutions increased to the highest values (Fig. 1a–c), indicating the complex formation, but the aggregation degree of the complexes (Fig. 1e) did not reach its maximum (compared to the particles produced after heating for 1 h), as we hypothesize that the MB synthesis involved preferentially small–-sized free–floating complexes rather than aggregated particles.

3.2. Synthesis, cytotoxicity study, and in vivo US imaging of BSA + pArg MB

The MB synthesis route is shown schematically in Fig. 2a and involves preheating a mixture of BSA and pArg solutions for 15 min in a water bath followed by 3 min of sonication to form MB, similarly to our previous reports [32]. The incorporation and uniform distribution of both BSA and pArg into the MB shell is demonstrated by confocal laser scanning microscopy (CLSM) (Fig. 2b) using BSA–FITC and pArg–TRITC conjugates. The lower intensity and width of the MB shell contour in the TRITC channel can be associated with a lower pArg concentration added during synthesis compared to the dominance of the BSA concentration.

The effect of the different molecular weight distributions of pArg used in the MB synthesis on the resulting MB yield, mean diameter distribution and shell thickness are presented in Table 1 (representative SEM images used for MB shell thickness quantification are shown in Fig. S4). As the pArg molecular weight distribution increased, the MB yield and mean diameters decreased, while all MB samples had mean diameters <2 μm. In contrast, MB shell thickness gradually increased with increasing pArg molecular weight distribution. Since the concentration of the intact components for MB synthesis was the same for all samples, we hypothesize a denser packing of complexes inside the MB shell, which may result in lower MB yield and higher MB shell thickness. Additionally, the introduction of pArg [15–70 kDa] resulted in the lower PDI values compared to other samples.

B–mode US was used to demonstrate MB echogenicity and to determine the optimal pArg molecular weight distribution (Fig. 3). As one can see in Fig. 3a, all MB samples showed significant echogenicity compared to the control saline solution, confirming successful air

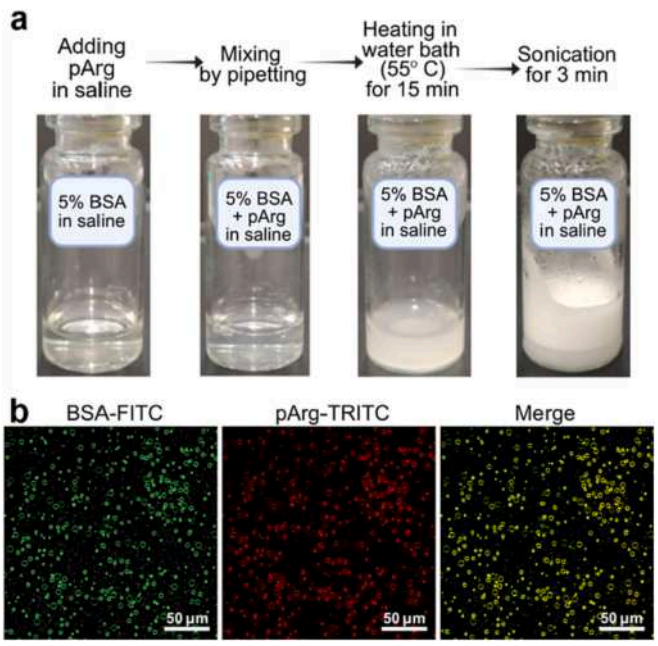

Fig. 2. Synthesis of BSA + pArg MB. (a) Vial photographs illustrating BSA + pArg MB synthesis steps. (b) Confocal laser scanning microscopy (CLSM) images of BSA + pArg MB prepared with BSA–FITC and pArg–TRITC conjugates in FITC, TRITC, and merged channels confirm the presence of both components in the MB shell.

Table 1
Characteristics of MB obtained with the addition of pArg of various molecular weights during the synthesis (BSA + pArg [5–15 kDa] MB, BSA + pArg [15–70 kDa] MB, and BSA + pArg [>70 kDa]) and without (plain BSA MB).

MB formulation	BSA MB	BSA + pArg [5–15 kDa] MB	BSA + pArg [15–70 kDa] MB	BSA + pArg [>70 kDa] MB
Yield, × 10^9 MB	1.5 ± 0.3	1.5 ± 0.2	1.1 ± 0.2	0.8 ± 0.6
Mean diameter, μm	1.6 ± 0.7	1.7 ± 0.9	1.6 ± 0.5	1.2 ± 0.5
PDI	0.44	0.53	0.31	0.42
Shell thickness, nm	22 ± 4	21 ± 2	36 ± 7	51 ± 9

entrapment inside MB shells. The analysis of mean US signal intensities provided in Fig. 3b highlights that BSA + pArg [15–70 kDa] MB showed the highest echogenicity compared to plain BSA MB and MB synthesized with pArg of different molecular weights. Therefore, we considered the pArg with moderate molecular weight distribution (pArg [15–70 kDa]) to be optimal for the MB synthesis, based on the low PDI values of MB, increased shell thickness, and improved US B–mode echogenicity compared to plain BSA MB counterparts.

Next, cytotoxicity experiments with BSA + pArg [15–70 kDa] MB (hereafter referred to as BSA–pArg MB) were performed to evaluate whether the selected MB composition has a negative effect on cell cultures. Since MB are commonly administered intravenously for contrast-enhanced ultrasound imaging, ensuring their compatibility with blood cells is critical. Therefore, the THP-1 (human monocyte cell line) was selected for testing. Representative images of THP–1 cells co–incubated with plain BSA MB (Fig. 4a) and BSA–pArg MB (Fig. 4b) demonstrate the preservation of the intact state of the cells and the absence of visually detectable deleterious effects on cells.

Cytotoxicity was assessed using the AlamarBlue assay, which is based on the degradation of resazurin to resorufin as a result of altered

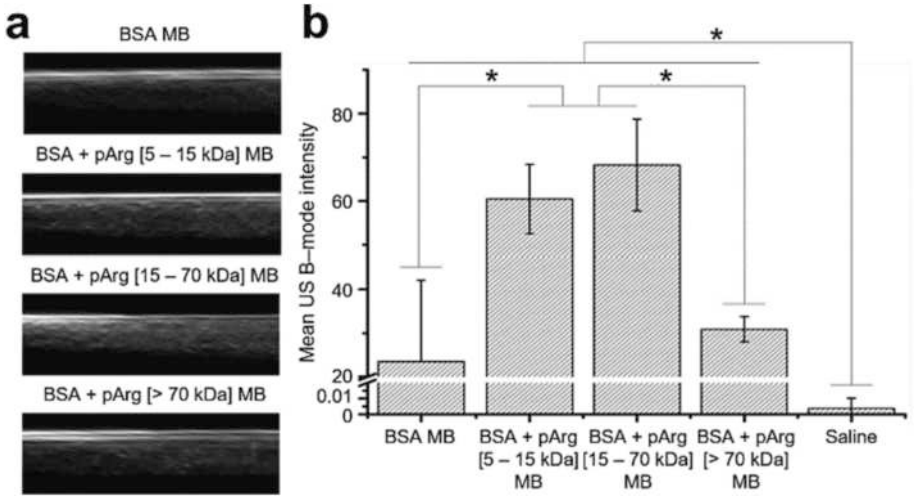

Fig. 3. US B–mode imaging of MB synthesized with pArg [5–15 kDa], [15–70 kDa], and [>70 kDa] in vessel mimicking phantoms. (a) Representative B–mode US images of plain BSA MB and BSA + pArg MB obtained by incorporating pArg of various molecular weight distributions into the MB shell structure. (b) The mean US B–mode intensities calculated by post–processing B–mode images. (*) indicates groups that are significantly different with $p < 0.05$ (one–way ANOVA with *post hoc* Tukey HSD test).

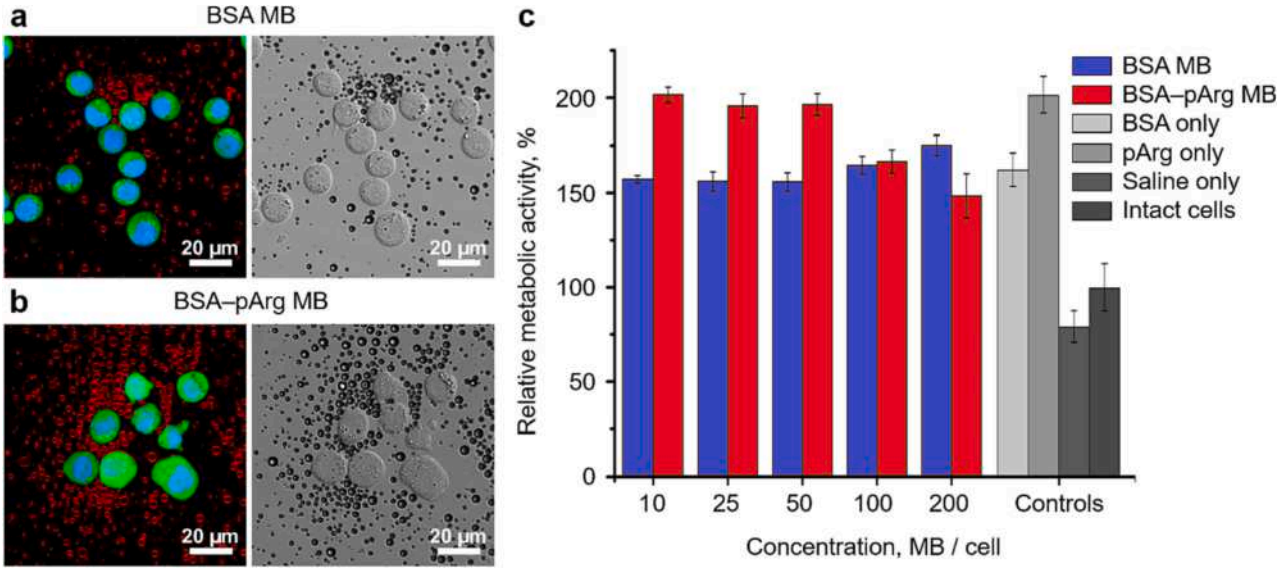

Fig. 4. Cytotoxicity evaluation of MB on THP–1 cells. CLSM images of (a) BSA MB and (b) BSA–pArg MB co–incubated with THP–1 cells. (c) Relative viability of THP–1 cells after co–incubation for 48 h with BSA MB, BSA–pArg MB, and corresponding shell materials used as controls.

metabolic activity of damaged cells. To evaluate the metabolic activity of MB shell components (taken as controls), we estimated the amount of BSA incorporated into MB using the Bradford protein assay (detailed description is presented in Supporting information, Section S2), which resulted in a concentration of 5 % compared to the amount of intact BSA (Fig. S5). Therefore, we considered 5 % of intact concentrations of BSA and pArg [15–70 kDa] as controls. As shown in Fig. 4c, no cytotoxicity was observed in any MB sample or intact shell material after co–incubation with cells for 48 h, as the resorufin–derived signal did not decrease. The signal increases for BSA–pArg MB and pArg, that might be related to the ability of pArg to increase the concentration of calcium ions inside cells and thereby increase cell metabolic activity (knowing that number of cells did not change during experiment) [44,45]. Therefore, even large numbers of MB per cell (up to 200 MB/cell) did not result in any toxic effects, which is consistent with recent reports on BSA MB [46,47].

Since MB are traditionally used for US imaging, we evaluated *in vivo* imaging capabilities after the injection of BSA–pArg MB into the jugular vein (Fig. 5a) or tail vein (Fig. 5f), by the MB movement (and associated increase in echogenicity in US B–mode) along the superior vena cava entering the heart (Fig. 5b–e) or inferior vena cava (Fig. 5g–h). During the first passage of MB through the observation point (near the injection site), a significant increase in US echogenicity (referred to as B–mode signal intensity) was noted compared to the signal from the vessel before injection. The US signal appeared almost immediately after the start of the injection, confirming the flow of MB within the vessel sufficient for detection in B–mode.

3.3. *Magnetic navigation of BSA + pArg MB functionalized with SPION*

We further functionalized BSA–pArg MB with magnetic nanoparticles (namely SPION) to endow MB with the capability of controlled movement under magnetic field guidance. SPION were adsorbed to BSA–pArg MB shells under gentle mixing, as schematically shown in

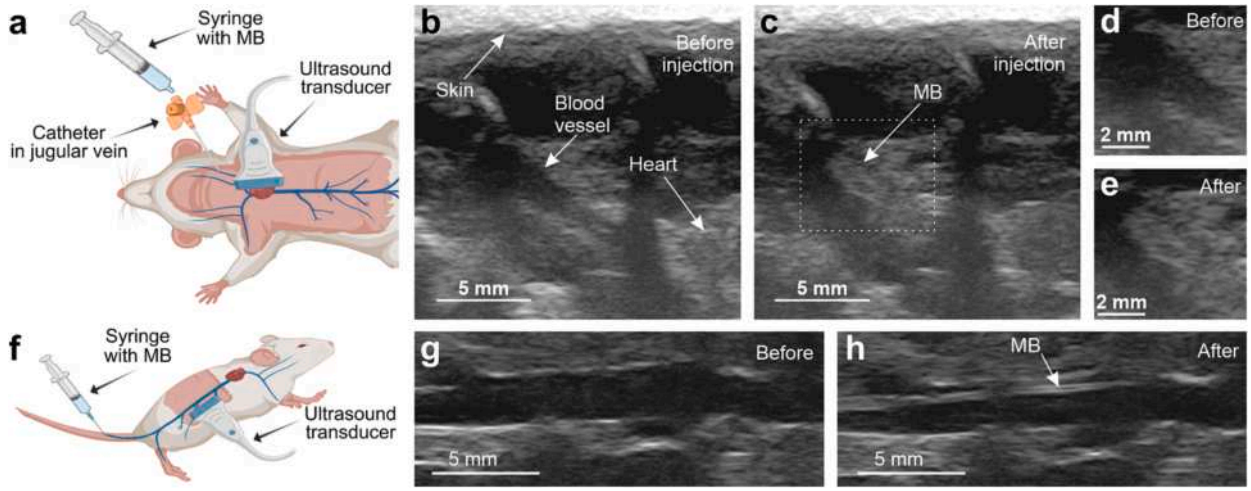

Fig. 5. *In vivo* US B–mode imaging (DUB Skinscanner, Taberna) of rat large vessels after the injection of BSA–pArg MB. (a) Schematic of MB injection into the jugular vein and observation of the superior vena cava flowing into the heart. Image was generated using Biorender.com. (b) US image of the heart area before MB injection. (c) US image of the heart area after MB injection. (d) US image of the superior vena cava before MB injection. (e) US image of the superior vena cava after MB injection. (f) Scheme of MB injection into the tail vein and observation of the inferior vena cava. Image was generated using Biorender.com. (g) US image of the area near the spine (below the ribs) before MB injection. (h) US image of the area near the spine (below the ribs) after MB injection.

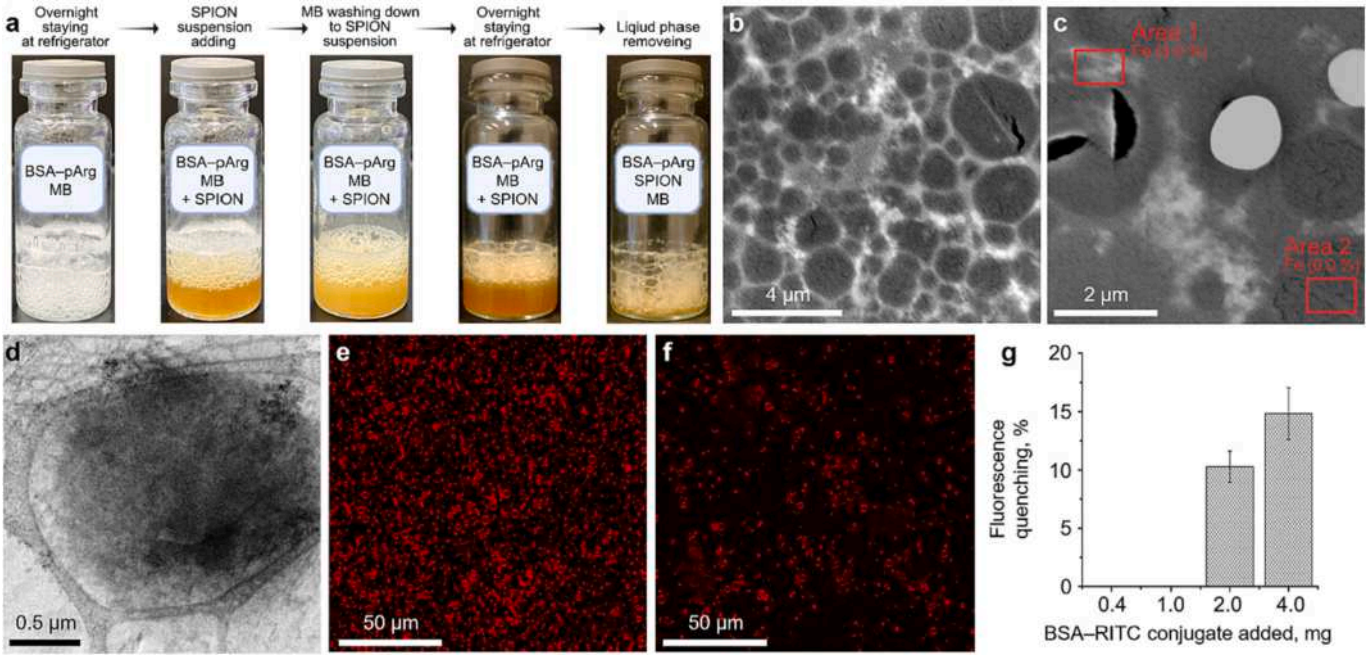

Fig. 6. BSA–pArg MB functionalization with SPION. (a) Vial photographs illustrating the steps of BSA–pArg MB functionalization with SPION. (b) Representative SEM image of MB functionalized with SPION. (c) Energy dispersive X–ray spectroscopy results of the percentage of Fe ions in the selected areas of the SEM images. (d) Representative cryoTEM image of MB functionalized with SPION. (e, f) CLSM images of BSA–pArg MB (e) before and (f) after adsorption of SPION into the MB shell. (g) Fluorescence quenching results of the RITC dye embedded in the MB shell after SPION adsorption of depending on the amount of BSA–RITC conjugate added during MB synthesis.

Fig. 6a, followed by several washing steps to remove unreacted components. Representative SEM image shown in Fig. 6b confirmed the SPION deposition in the MB shells, as bright, almost white dots and areas correspond to heavier Fe atoms compared to lighter H, C, and N atoms of the BSA and pArg counterparts. Energy dispersive X–ray spectroscopy confirmed that the brightest regions contain Fe atoms associated with SPION (Figs. 6c, SI6, SI7). Also, SPION deposition was confirmed with cryoTEM (Fig. 6d). During *in vitro* US imaging studies, MB do not lose their echo contrast properties after functionalization with SPION (Fig. SI.8). The mean US B-mode intensity slightly decreased compared to plain MB, which may be due to a reduce in the number of MB after functionalization.

Fig. 6e and f shows CLSM images of BSA–pArg MB with RITC embedded in the shell before and after SPION adsorption, respectively. The signal intensities in the presented images correlated with the fact that after the SPION deposition in MB shells the resulting MB concentration was 60–65 % compared to the intact MB suspension. However, SPION may additionally quench the dye signal after the dense packing of both additives in the MB shell if the distance between them is of several nanometers [48,49]. Therefore, we evaluated the fluorescence quenching for a set of BSA–RITC concentrations incorporated into MB shells by comparing the averaged signal intensities of the dye before and after

SPION deposition at fixed MB concentration. As can be seen in Fig. 6g, quenching did not occur at low amounts of dye and the effect increased with increasing amounts of rhodamine immobilized in the shell. This may be related to the close proximity of the fluorophore and the SPION in MB shells: the less dye is added to the shell, the less likely the dye and the SPION would be close to each other, and the less effect the SPION would have on the fluorescence intensity.

Next, we determined the magnetic moment and magnetic polarizability values for a single MB using the optical tweezers method described by Vavaev, et al [34] The average amplitude of the magnetic moment of the MB was evaluated using Eq. (S9) (described in Supporting information, Section S1) and turned out to be $(1.79 \pm 0.21) \times 10^{-15}$ A·m^2. Using the magnetic moment determined in the experiment, we calculated the magnetization of the single MB using Eq. (S11) (Supporting information, Section S1): the resulting value is $(3.6 \pm 0.4) \times 10^{-19}$ m^3.

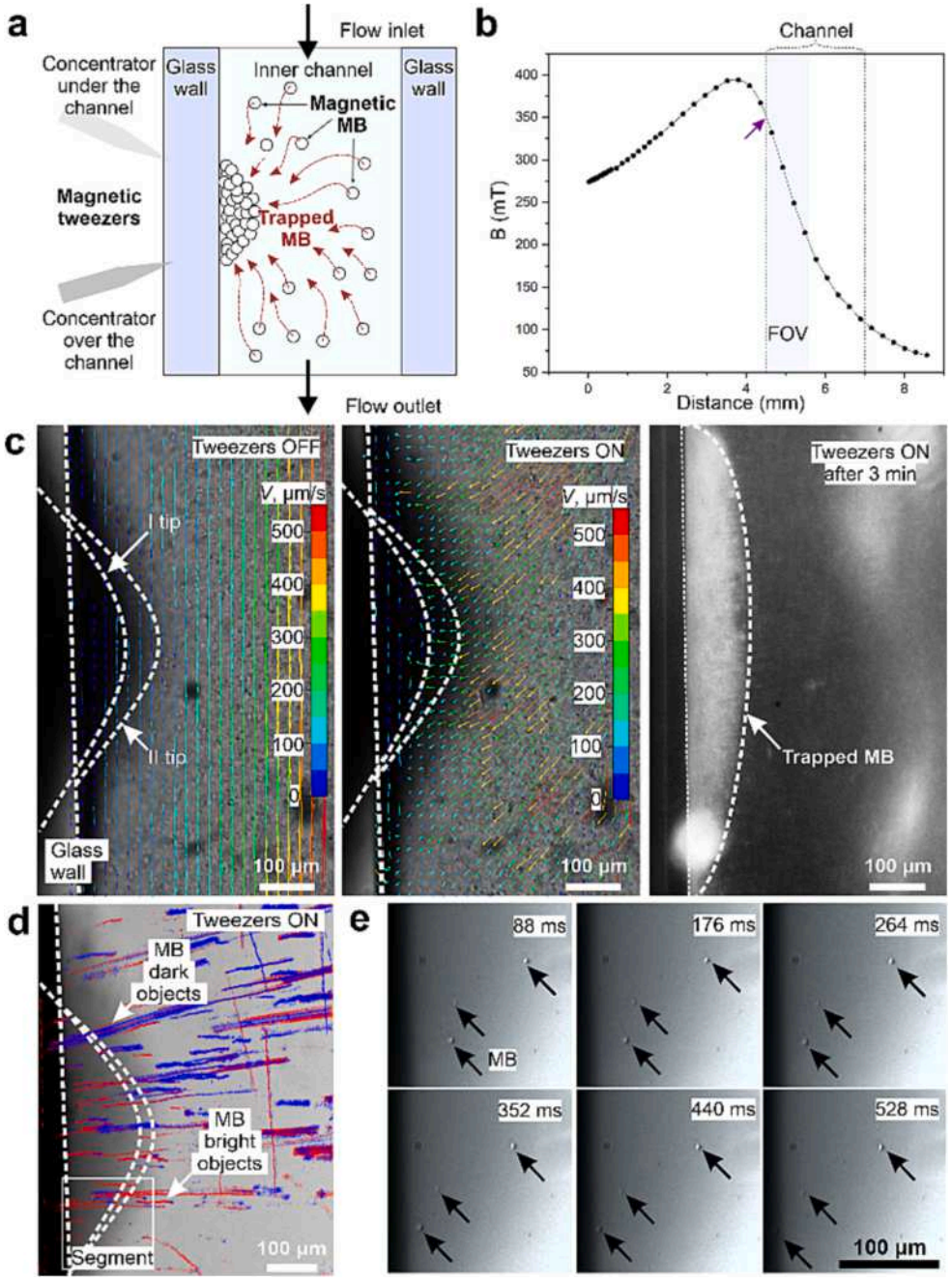

Fig. 7. *In vitro* magnetic entrapment of SPION–functionalized BSA–pArg MB with magnetic tweezers. (a) Schematic diagram of the setup used: MB suspension is pumped through the capillary phantom with a constant flow rate, while magnetic tweezers modify the MB flow trajectories and trap MB at the region of interest by electromagnetic forces. (b) Diagram of the magnetic field induction (B) distribution in the tweezers gap. The purple arrow indicates the position of the edge of the magnetic sensor, which is on the straight line connecting the tweezer tips. Dashed lines mark the dimensions of the inner channel of the capillary relative to the position of the tweezer tips. A field of view (FOV) indicates the capillary area observed by the microscope. (c) Demonstration of MB magnetic entrapment: MB float through the phantom with rectilinear trajectories while the tweezers are turned off, while the introduction of a magnetic field can change the MB trajectories and velocities toward the region of interest, resulting in MB magnetic entrapment within 3 min. (d) Tracking of individual MB trajectories under the action of a gradient magnetic field. (e) Demonstration of individual MB movement toward the tips of the tweezers. (For interpretation of the references to color in this figure legend, the reader is referred to the web version of this article.)

In vitro magnetic entrapment of MB was performed using electromagnetic tweezers and a vessel mimicking phantom (Fig. 7). Magnetic MB were pumped through the capillary at a constant flow rate, while the introduction of tweezers allowed us to trace the dynamics of individual MB movement under the influence of the magnetic field gradient and to accumulate MB in the desired area, as schematically shown in Fig. 7a. The magnetic field induction in the trapping area was 370 mT (Fig. 7b).

To demonstrate the MB magnetic entrapment, we pumped the MB suspension with an initial concentration of 4×10^8 MB/mL through the phantom capillary and imaged the MB movement using particle image velocimetry with and without an external magnetic field influence (Fig. 7c). When the tweezers were turned off ("Tweezers OFF" in Fig. 7c), the MB velocity distributions followed Poiseuille laws, and the velocity vectors of the MB motion corresponded to the direction of fluid motion. After the magnetic field was activated ("Tweezers ON"), the direction of MB motion deviated from a straight motion along the liquid flow and began to be pulled toward the area where the tweezer tips were placed along the gradient of the magnetic field, resulting in the MB magnetic entrapment. After 3 min of magnetic field application, the magnetic capture target area was filled with captured MB.

To image the individual trajectories of a single MB, we diluted the MB suspension to a concentration of 1×10^8 MB/mL and applied MB motion analysis to 700 images at 114 fps. A representative image with trajectory analysis is shown in Fig. 7d. In each consecutive frame, individual MB were detected by bright moving objects (shown as red patterns in Fig. 7d) and dark moving objects (shown as blue patterns in Fig. 7d), and then plotted together. Further dilution of the MB suspension to a concentration of 1×10^5 MB/mL allowed us to image the frame–by–frame motion of three individual isolated magnetic MB in the segment highlighted in Fig. 7e. Differences in MB displacements may indicate the heterogeneous distribution of SPION in MB shells within a single MB population.

The possibility of magnetic MB navigation to the region of interest under the magnetic field exposure was also demonstrated by co–incubation of a RenCa cells (mouse renal carcinoma cells) and MB. RenCa cell line was chosen as a cancerous model and one of adherent culture line that in ordinary conditions *in vitro* was opposite to MB (RenCa was on the bottom of Chambered Coverglass, MB was near the liquid-air surface of the culture media). RenCa cells were grown in opposite wells of Chambered Coverglass and later supplemented with SPION–functionalized BSA–pArg MB. BSA–RITC conjugate was incorporated into the MB shells for CLSM imaging. One well of Chambered Coverglass was left to incubate at room temperature without exposure to a magnetic field, and a permanent magnet was placed under the bottom of the other well. After 10 min of co–incubation, the Chambered Coverglass was transferred to the CLSM and volumetric images were taken (from the bottom of the well, where the adherent culture was located, to the top liquid surface) (Figs. 8 and S9). Unlike polymeric particles or capsules of similar size that sediment in the liquid, MB are filled with air and will therefore float to the air–liquid interface of a solution, making it highly unlikely that MB will be detected at the bottom of the well without external influence (Fig. 8a). In contrast, MB can be navigated against buoyancy to the bottom of the Chambered Coverglass by applying an external gradient magnetic field (Fig. 8b).

After magnetic localization of SPION–functionalized BSA–pArg MB at the bottom part of the Chambered Coverglass, we additionally examined MB interactions by RenCa cells over longer periods of time, as MB can degrade into particles or capsules by gas core dissolution or undergo cell uptake (Fig. 9). To distinguish MB and particles, it can be noted that in a brightfield mode MB have a dark core and a bright shell, while particles appear as bright objects of irregular shape (Fig. S10). In addition, the fluorescence of particles can be significantly higher than the fluorescence of the MB shell because particles are more likely to have a denser packing of components (including fluorescent labels) in their

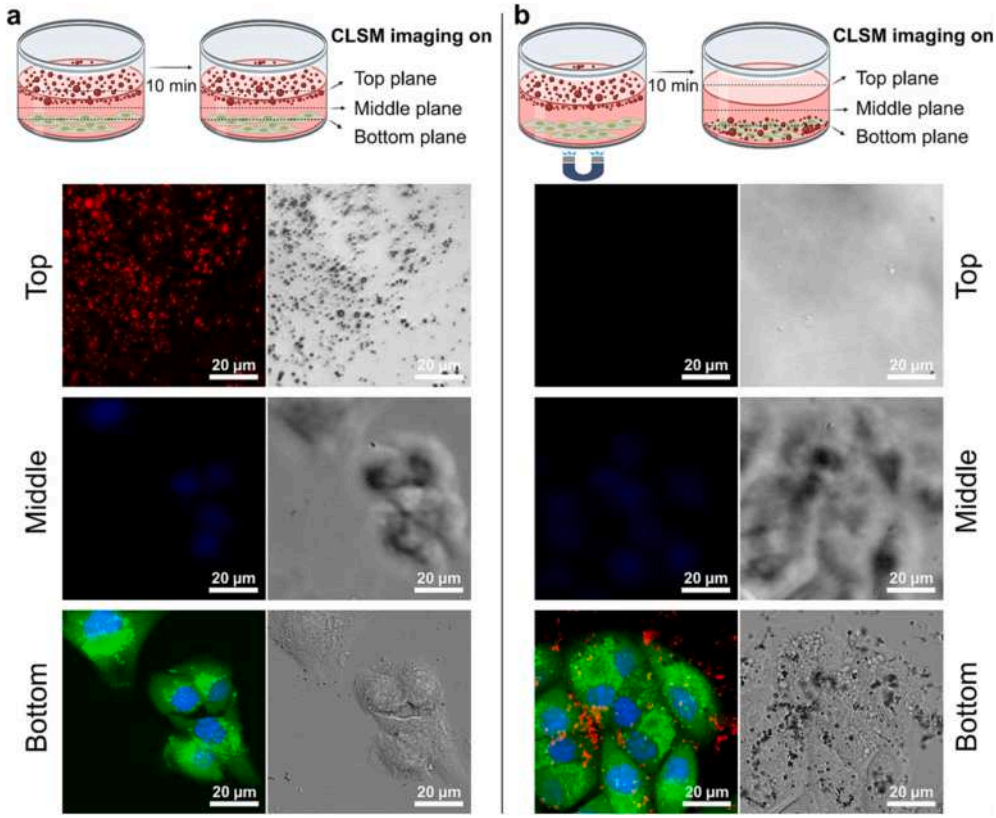

Fig. 8. *In vitro* magnetic navigation of SPION–functionalized BSA–pArg MB during co–incubation with RenCa cells. Scheme of the experiment and CLSM images of top, middle, and bottom parts of the well of Chambered Coverglass after 10 min of co–incubation of RenCa cells and magnetic MB (a) without and (b) with exposure to an external magnetic field. Corresponding 3D reconstructions of the CLSM images are shown in Fig. S6.

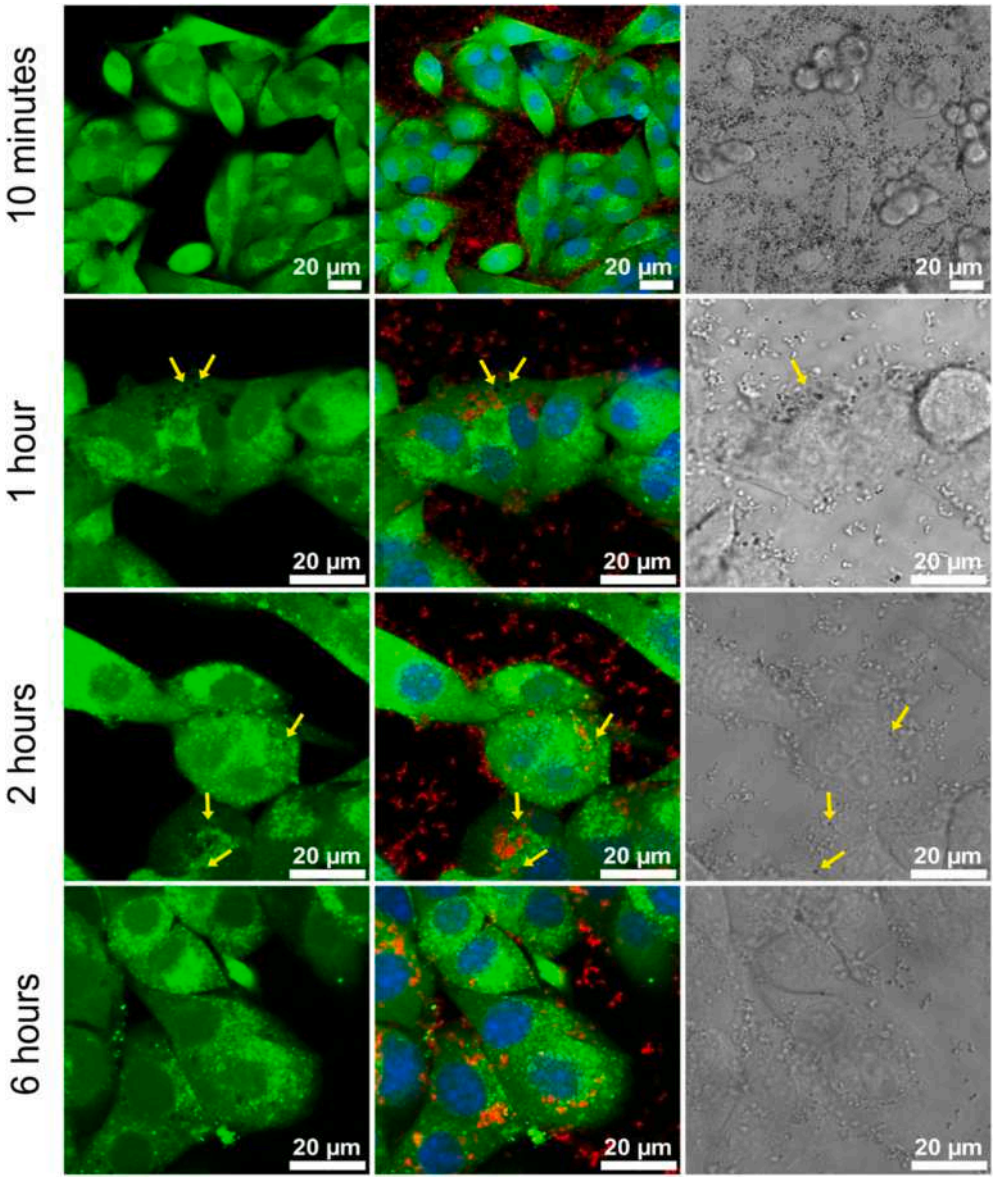

Fig. 9. Interactions of SPION–functionalized BSA–pArg MB with RenCa cells at 10 min, 1 h, 2 h, and 6 h after magnetic co–localization. Cytoplasm was stained with Calcein AM (green channel), MB shell was stained with RITC (red channel), nucleus was stained with Hoechst (blue channel). Yellow arrows highlight events of MB uptake by cells with the preserved gaseous core. (For interpretation of the references to color in this figure legend, the reader is referred to the web version of this article.)

structure compared to the MB shell. In addition, slow dissolution of the MB air core followed by replacement by the surrounding liquid can result in capsules that do not have a dark core in the brightfield mode but retain a spherical shape and a slightly light shell preserved from intact MB (Fig. S10).

After 1 h of co–incubation, the cells absorbed some MB (indicated by yellow arrows in Fig. 9). This is evidenced by the circular regions within the cell cytoplasm that lack Calcein AM staining in the green channel. In addition, no fluorescence was observed in the red and blue channels. These circular areas retained a dark appearance surrounded by a small, bright shell in the bright field, corresponding to the MB air nucleus. Such intracellular structures were not seen in images of cells taken after 10 min of co–incubation, as this time point was not sufficient enough for MB internalization. In contrast, when the particles (not MB) were internalized, the unstained Calcein AM region was filled with a signal from the BSA–RITC conjugate (originally introduced in the MB shell composition). After 6 h of incubation, there were no areas inside the cells that showed no fluorescence in either the green or red channel corresponding to Calcein AM or RITC, respectively (Fig. 9).

To demonstrate the advantages of magnetic MB co–localization with cells, SPION–loaded MB were prepared using BSA–Dox complex to study DOX–induced cytotoxicity on RenCa cells. The experimental design involved magnetic navigation of MB to the bottom of one of four glass chambers or groups of wells of a 96–well plate, compared to the group in which MB were allowed to float freely to the top. After 30 min of co–incubation of cells with MB, the 70 % portion of the culture medium was carefully removed from the top of all wells or chambers and replaced with fresh medium. The wells were then left for further analysis. Fig. 10a highlights the cytotoxic effect of DOX–loaded magnetic MB when the external magnetic field source was applied compared to the group treated with free–floating MB (without magnetic gradient) and control cells. Magnetic co–localization of MB and cells promoted a significant cytotoxic effect at 48 and 72 h after treatment, which is comparable to reports on US–mediated destruction of DOX–loaded MB [50,51]. Representative CLSM images obtained 30 min, 24, 48, and 72 h after treatment are shown in Fig. 10b, while corresponding brightfield

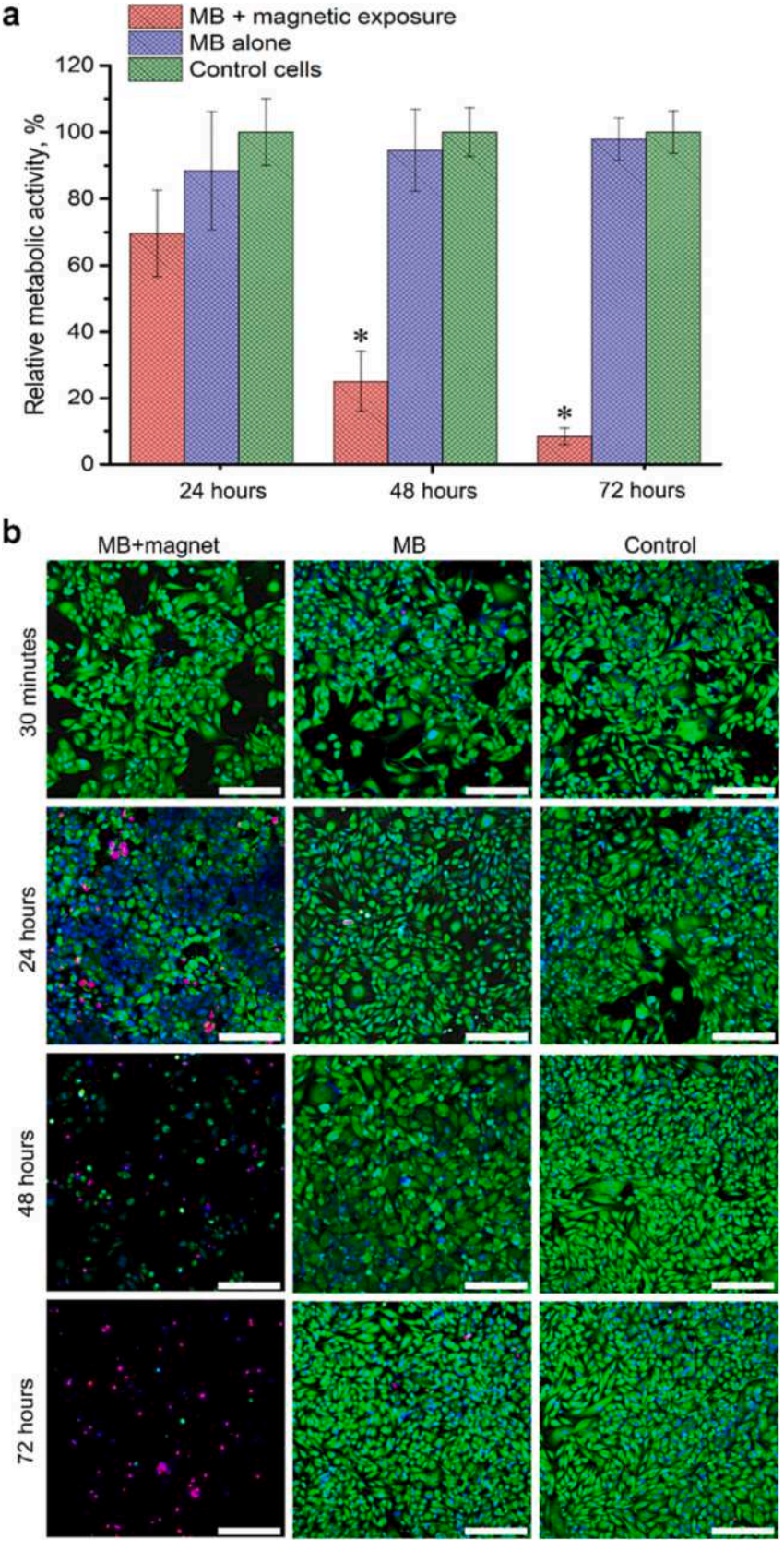

(caption on next page)

Fig. 10. Cytotoxic effect of DOX–loaded magnetic MB promoted by magnetic co–localization of MB and RenCa cells. (a) Metabolic activity of RenCa cells 24, 48 and 72 h after the treatment initiation. The groups were divided into RenCa cells treated with Dox MB magnetic co–localization, freely floating Dox MB without any magnetic field source applied, and control cells that received no treatment. (b) Corresponding CLSM micrographs taken 30 min, 24, 48, and 72 h after the treatment initiation. Blue color represents nuclear staining with Hoechst, green represents cytosol of viable cells stained with Calcein AM, red represents PI incorporation into nuclei of cells with damaged membranes. The magenta color corresponds to the overlay of blue and red colors. (*) indicates groups that are significantly different with $p < 0.05$ (one–way ANOVA with *post hoc* Tukey HSD test). The corresponding brightfield micrographs are shown in Fig. S11. (For interpretation of the references to color in this figure legend, the reader is referred to the web version of this article.)

micrographs are shown in Fig. S11. At the 30–minute time point, MB treated with an external magnetic field source were localized at the bottom of the chambered glass in proximity to cells (therefore, can be seen in Fig. S8), compared to cells that were free of any particles in the chamber for groups treated with MB alone or taken as control. PI staining was negligible at the 30 minute time point (Fig. 10b), indicating that the cell populations were viable immediately after treatment. However, cytotoxic activity appeared 24 h after treatment in the group where cells were co–localized with Dox–loaded MB, as indicated by a decrease in metabolic activity and an increase in PI staining combined with a decrease in the intensity of Calcein AM, as shown in Fig. 10a and b, respectively. A sharp decrease in the amount of viable cells for the magnetic co–localization group was observed at 48 and 72 h after treatment, highlighted by a drastic increase in PI staining and a reduction in the number of cells stained with Calcein AM. Interestingly, a slight decrease in the number of cells was observed in the MB alone group 48 h after treatment. We hypothesize that a partial release of Dox from the MB shells into the culture medium may occur, but such an effect did not show statistical significance (Fig. 10a). At the 72–hour time point, the number of viable cells and the intensity of Calcein AM cell staining for the free–floating Dox MB group were comparable to the control cells.

Therefore, we demonstrated a successful SPION functionalization of BSA–pArg MB shells, which allowed us to perform *in vitro* magnetic navigation of modified MB both in a vascular mimicking phantom using magnetic tweezers and in co–incubation with RenCa cells by applying an external magnetic field. The advantages of such controlled localization and the efficacy of suppressing cancer cell growth using MB containing a cytotoxic drug and SPION were demonstrated with *in vitro* experiments on RenCa cells.

4. Discussion

Efficient and intense complexation of BSA + pArg was induced by heating a mixture of BSA and pArg solutions in a water bath and was confirmed by an increase in the optical density of the mixture (Fig. 1a–c) and the SEM observation of submicron–sized aggregates with moderate polydispersity (Fig. 1e), which is in line with current developments in protein–polymer complex–based nanoparticles aimed for drug delivery [52,53]. Similar temperature and pH conditions have been previously reported for the formation of BSA nanoparticles instead of amorphous aggregation of the protein [54]. We hypothesize that gentle preheating at 55 °C can slightly destabilize the secondary and local tertiary structures of BSA, facilitating electrostatic interactions with pArg and thereby promoting BSA + pArg complexation. The proposed mechanism is in agreement with the report on the complexation of BSA with polysaccharides [55]. Successful complex formation can be achieved within 15 min, as observed by the relatively high optical densities of the complexes for all molecular weight distributions of pArg considered. Therefore, we considered this time point as optimal for further MB synthesis based on BSA + pArg complexes.

After MB were synthesized by sonication as shown schematically in Fig. 2a, CLSM images confirmed the incorporation and uniform distribution of BSA and pArg components into the MB shell (Fig. 2b). Molecular weight distributions of pArg showed an effect on MB physicochemical properties, including MB yield, mean diameter, shell thickness (Table 1), with the MB composition based on pArg [15–70 kDa] showing the narrowest polydispersity, which may promote greater US response sensitivity compared to polydisperse counterparts [56,57]. While the mean diameters of plain BSA MB and BSA + pArg [15–70 kDa] MB were similar, allowing us to accurately compare their *in vitro* US B–mode echogenicity, pArg–modified MB had thicker MB shells (Table 1), which may indicate the role of pArg in promoting MB shell stability, as thicker MB shells are more difficult to destroy by US [10,58]. Overall, BSA + pArg [15–70 kDa] MB exhibited the highest *in vitro* echogenicity compared to other pArg–based and plain BSA MB counterparts, suggesting this sample as optimal for further consideration. Further *in vivo* observations of BSA–pArg MB echogenicity during motion in large vessels during B–mode US imaging (Fig. 5) confirmed the potential use of the proposed formulation as contrast agent for US imaging.

Assessment of the metabolic activity of THP–1 cells co–incubated with BSA MB and BSA–pArg MB showed no significant cytotoxicity (Fig. 4c). Surprisingly, increase in the concentration of BSA MB per cell resulted in a slight increase in metabolic activity, but increase in the concentration of BSA–pArg MB resulted in a significant decrease in metabolic activity (compared to low concentrations for this MB composition). We hypothesize that one of the reasons for this is that MB shells can degrade into BSA + pArg aggregates during prolonged co–incubation with cell lines, as we observed later with RenCa cells (Fig. 9).

Further modification of BSA–pArg MB with SPION, confirmed by SEM and cryoTEM images (Fig. 6b and d, respectively), as well as direct evaluation of a magnetic moment of individual MB trapped by optical tweezers, allowed us to magnetically navigate them in a controlled manner. At increased amounts of BSA–RITC conjugate incorporated in MB shells, SPION deposition could facilitate fluorescence quenching of the fluorophore (Fig. 6g), which correlates with previous reports on microcapsules loaded with SPION and fluorophores [49,59].

The magnetic moment values of individual MB were comparable with recently described values for magnetic lipid MB of 3 μm and polymeric capsules of 0.5 μm functionalized with SPION [29,34]. Thereby, we demonstrated *in vitro* MB magnetic navigation in the vessel mimicking phantom using magnetic tweezers (Fig. 7) and during co–incubation with RenCa cells (Fig. 8) by applied external magnetic field. To our knowledge, this is the first example of magnetic navigation with shell–coated MB and magnetic tweezers. Together with a recent example of magneto–acoustic device implementation on MB [30], this opens up possibilities of SPION–functionalized MB direct manipulation with magnetic fields, preserving their acoustic responsiveness.

As demonstrated in Fig. 9, MB were able to internalize after magnetically induced co–localization of MB and cells. Presumably, MB retain their structure inside the phagocytic vesicle for a very short time, because after fusion with the lysosome, whose pH is in the acidic range [60], the MB shell packing tends to be destroyed under the action of pH and various enzymes. It correlated with the MB elimination detected during long–term monitoring of phagocytic Kupffer cells [61]. Along with MB, the cells were loaded with significant amounts of BSA + pArg particles derived from MB shells. Therefore, cells were able to internalize MB while maintaining MB shape, while the majority of MB shells were destroyed over time, and derived particles were more efficiently taken up by cells.

To demonstrate the therapeutic potential of magnetic MB co–localization with cells, we synthesized Dox– and SPION–loaded MB and conducted the experiment on the cytotoxic effect promoted by magnetic co–localization of such MB constructs and cells. The

experiment was aimed to mimic the effect of environmental renewal *in vivo*, such as in blood vessels. The complexation of Dox with BSA prior to MB synthesis is consistent with the recent report on maximizing anthracycline drug loading in albumin MB [62]. As shown in Fig. 10, magnetic co–localization of drug–loaded MB with cells induced a significant cytotoxic effect compared to groups of freely floated MB (with no magnetic field gradient applied) and control cells. Such magnetic targeting strategy may be beneficial in reducing tumor cell growth by direct navigation of drug carriers [18,30,63], as well as reducing the known side effects of systemic administration of anthracyclines [64,65].

For further development, we envision that direct magnetic navigation of SPION-functionalized MB could potentiate molecular imaging and drug delivery approaches (where MB compositions would additionally include targeting ligands or therapeutic cargos), as well as vesicle separation strategies.

5. Conclusions

In summary, we demonstrated *in vitro* magnetic navigation with developed MB composition consisting of a hybrid BSA + pArg shell functionalized with SPION. We identified the optimal conditions for complexation of BSA and pArg of different molecular weight distributions followed by MB synthesis and showed that pArg of moderate molecular weight distribution [15–70 kDa] provided MB with enhanced shell stability, significant *in vitro* and *in vivo* acoustic response, and no cytotoxicity after 48 h of incubation with THP-1 cells. Once SPION were adsorbed on BSA + pArg MB shells, we calculated the magnetic moment values provided by individual MB and demonstrated the controlled magnetic navigation in a vessel mimicking phantom using magnetic tweezers and co-incubation with RenCa cell culture using an applied magnetic field gradient. After magnetic co-localization of SPION-functionalized MB and RenCa cells, several MB were able to internalize and retain their gaseous core for up to 2 h. The *in vitro* experiments on RenCa cells demonstrated the effectiveness of MB containing a cytotoxic drug and SPION in suppressing cancer cell growth, showcasing the benefits of controlled localization. Taken together, these results highlight the advantages of tuning MB shell composition by protein–polymer complex incorporation and magnetic navigation of SPION-loaded MB, which can be further used for US combined with magnetic resonance imaging, drug delivery, and extracellular vesicles isolation and magnetic/acoustic manipulation.

Abbreviations

US	Ultrasound
MB	Microbubbles
BSA	Bovine serum albumin
pArg	Poly–L–arginine
pArg [5–15 kDa]	Poly–L–arginine with molecular weight 5–15 kDa
pArg [15–70 kDa]	Poly–L–arginine with molecular weight 15–70 kDa
pArg [>70 kDa]	Poly–L–arginine with molecular weight > 70 kDa
RITC	Rhodamine B isothiocyanate
FITC	Fluorescein 5(6) isothiocyanate
TRITC	Tetramethylrhodamine isothiocyanate
SPION	Superparamagnetic iron oxide nanoparticles
DMEM	Dulbecco's modified Eagle medium
RPMI-1640	Roswell Park Memorial Institute medium
FBS	Fetal bovine serum
HBSS	Hanks' balanced salt solution
DLS	Dynamic light scattering
PDI	Polydispersity index
CLSM	Confocal laser scanning microscopy
SEM	Scanning electron microscopy
CryoTEM	Transmission electron cryomicroscopy
THP-1	Human monocyte suspension cell line
RenCa	Mouse renal carcinoma cell line
DI	Deionized water
PI	Propidium Iodide

CRediT authorship contribution statement

Olga I. Gusliakova: Writing – original draft, Validation, Resources, Methodology, Investigation, Formal analysis, Conceptualization. **Maxim A. Kurochkin:** Writing – original draft, Visualization, Software, Investigation, Formal analysis, Conceptualization. **Roman A. Barmin:** Writing – original draft, Validation, Methodology, Investigation, Conceptualization. **Ekaterina S. Prikhozhdenko:** Visualization, Resources, Investigation, Formal analysis, Data curation. **Tatyana M. Estifeeva:** Investigation. **Polina G. Rudakovskaya:** Methodology, Investigation. **Olga A. Sindeeva:** Visualization, Investigation. **Victor V. Galushka:** Visualization, Investigation. **Evgeny S. Vavaev:** Visualization, Software, Investigation, Data curation. **Aleksei S. Komlev:** Software, Investigation, Data curation. **Evgeny V. Lyubin:** Investigation, Data curation. **Andrey A. Fedyanin:** Writing – review & editing, Supervision. **Krishna Kanti Dey:** Writing – review & editing, Supervision. **Dmitry A. Gorin:** Writing – review & editing, Supervision, Resources, Project administration, Funding acquisition.

Declaration of competing interest

The authors declare that they have no known competing financial interests or personal relationships that could have appeared to influence the work reported in this paper.

Data availability

Data will be made available on request.

Acknowledgements

This work was supported by the Russian Foundation for Basic Research (RFBR grant 19-53-80047 BRICS_t), Ministry of Science and Higher Education of the Russian Federation within the framework of a state assignment (project No. FSRR-2023-0007), and Department of Science and Technology, Govt. of India (DST/ICD/BRICS/PilotCall3/BioTheraBubble/2019). This work was supported by Clover Program: Joint Research Projects of Skoltech, MIPT, and ITMO University. Some figure panels were generated using Biorender.com.

Appendix A. Supplementary data

Supplementary data to this article can be found online at https://doi.org/10.1016/j.bioadv.2024.213759.

References

[1] S. Mitragotri, Healing sound: the use of ultrasound in drug delivery and other therapeutic applications, Nat. Rev. Drug Discov. 4 (2005) 255–260, https://doi.org/10.1038/nrd1662.
[2] P.N.T. Wells, Ultrasound imaging, Phys. Med. Biol. 51 (2006) R83, https://doi.org/10.1088/0031-9155/51/13/R06.
[3] J.R. Lindner, Microbubbles in medical imaging: current applications and future directions, Nat. Rev. Drug Discov. 3 (2004) 527–533, https://doi.org/10.1038/nrd1417.
[4] K. Kooiman, H.J. Vos, M. Versluis, N. de Jong, Acoustic behavior of microbubbles and implications for drug delivery, Adv. Drug Deliv. Rev. 72 (2014) 28–48, https://doi.org/10.1016/j.addr.2014.03.003.
[5] E. Stride, et al., Microbubble agents: new directions, Ultrasound Med. Biol. 46 (1326–1343) (2020) 1326–1343, https://doi.org/10.1016/j.ultrasmedbio.2020.01.027.
[6] S. Hernot, A.L. Klibanov, Microbubbles in ultrasound-triggered drug and gene delivery, Adv. Drug Deliv. Rev. 60 (2008) 1153–1166, https://doi.org/10.1016/j.addr.2008.03.005.
[7] S.R. Sirsi, M.A. Borden, Microbubble compositions, properties and biomedical applications, Bubble Sci. Eng. Technol. 1 (2009) 3–17, https://doi.org/10.1179/175889709X446507.

[8] P. Koczera, et al., PBCA-based polymeric microbubbles for molecular imaging and drug delivery, J. Control. Release 259 (2017) 128–135, https://doi.org/10.1016/j.jconrel.2017.03.006.

[9] P.G. Rudakovskaya, et al., Microbubbles stabilized by protein shell: from pioneering ultrasound contrast agents to advanced theranostic systems, Pharmaceutics 14 (2022) 1236, https://doi.org/10.3390/pharmaceutics14061236.

[10] R.A. Barmin, et al., Engineering the acoustic response and drug loading capacity of PBCA-based polymeric microbubbles with surfactants, Mol. Pharm. 19 (2022) 3256–3266, https://doi.org/10.1021/acs.molpharmaceut.2c00416.

[11] R.A. Barmin, et al., Enhanced stable cavitation and nonlinear acoustic properties of poly(butyl cyanoacrylate) polymeric microbubbles after bioconjugation, ACS Biomater. Sci. Eng. (2022), https://doi.org/10.1021/acsbiomaterials.2c01021.

[12] R.A. Barmin, et al., Polymeric materials for ultrasound imaging and therapy, Chem. Sci. 14 (2023) 11941–11954, https://doi.org/10.1039/d3sc04339h.

[13] Y. Chen, et al., Lipid/PLGA hybrid microbubbles as a versatile platform for noninvasive image-guided targeted drug delivery, ACS Appl. Mater. Interfaces 11 (2019) 41842–41852, https://doi.org/10.1021/acsami.9b10188.

[14] T.M. Estifeeva, et al., Hybrid (bovine serum albumin)/poly(N-vinyl-2-pyrrolidone-co-acrylic acid)-shelled microbubbles as advanced ultrasound contrast agents, ACS Appl. Bio Mater. (2022), https://doi.org/10.1021/acsabm.2c00331.

[15] N.H. Tsao, E.A.H. Hall, Enzyme-degradable hybrid polymer/silica microbubbles as ultrasound contrast agents, Langmuir 32 (2016) 6534–6543, https://doi.org/10.1021/acs.langmuir.6b01075.

[16] H. Hu, J. Quintana, R. Weissleder, S. Parangi, M. Miller, Deciphering albumin-directed drug delivery by imaging, Adv. Drug Deliv. Rev. 185 (2022) 114237, https://doi.org/10.1016/j.addr.2022.114237.

[17] Sasidharan, S., Bahadur, D. & Srivastava, R. Protein-poly(amino acid) nanocore–shell mediated synthesis of branched gold nanostructures for computed tomographic imaging and photothermal therapy of cancer. ACS Appl. Mater. Interfaces 8, 15889–15903 (2016). doi:https://doi.org/10.1021/acsami.6b03428.

[18] O.A. Mayorova, et al., Endovascular addressing improves the effectiveness of magnetic targeting of drug carrier. Comparison with the conventional administration method. Nanomedicine Nanotechnology, Biol. Med. 28 (2020) 102184, https://doi.org/10.1016/j.nano.2020.102184.

[19] M.V. Novoselova, et al., Biodegradable polymeric multilayer capsules for therapy of lung cancer, ACS Appl. Mater. Interfaces 12 (2020) 5610–5623, https://doi.org/10.1021/acsami.9b21381.

[20] Y. Tarakanchikova, et al., Biodegradable nanocarriers resembling extracellular vesicles deliver genetic material with the highest efficiency to various cell types, Small 16 (2020) 1904880, https://doi.org/10.1002/smll.201904880.

[21] K. Kubiak-Ossowska, B. Jachimska, P.A. Mulheran, How negatively charged proteins adsorb to negatively charged surfaces: a molecular dynamics study of BSA adsorption on silica, J. Phys. Chem. B 120 (2016) 10463–10468, https://doi.org/10.1021/acs.jpcb.6b07646.

[22] Mujtaba, J. et al. Micro-bio-chemo-mechanical-systems: micromotors, microfluidics, and nanozymes for biomedical applications. Adv. Mater. 33, 2007465 (2021). https://doi.org/10.1002/adma.202007465.

[23] X. Cai, F. Yang, N. Gu, Applications of magnetic microbubbles for theranostics, Theranostics 2 (2012) 103–112, https://doi.org/10.7150/thno.3464.

[24] A. Jameel, P. Bain, D. Nandi, B. Jones, W. Gedroyc, Device profile of exAblate Neuro 4000, the leading system for brain magnetic resonance guided focused ultrasound technology: an overview of its safety and efficacy in the treatment of medically refractory essential tremor, Expert Rev. Med. Devices 18 (2021) 429–437, https://doi.org/10.1080/17434440.2021.1921572.

[25] T.B. Brismar, et al., Magnetite nanoparticles can be coupled to microbubbles to support multimodal imaging, Biomacromolecules 13 (2012) 1390–1399, https://doi.org/10.1021/bm300099f.

[26] E. Beguin, L. Bau, S. Shrivastava, E. Stride, Comparing strategies for magnetic functionalization of microbubbles, ACS Appl. Mater. Interfaces 11 (2019) 1829–1840, https://doi.org/10.1021/acsami.8b18418.

[27] T. Lammers, et al., Theranostic USPIO-loaded microbubbles for mediating and monitoring blood-brain barrier permeation, Adv. Funct. Mater. 25 (2015) 36–43, https://doi.org/10.1002/adfm.201401199.

[28] V. Pathak, et al., Molecular magnetic resonance imaging of Alpha-v-Beta-3 integrin expression in tumors with ultrasound microbubbles, Biomaterials 275 (2021) 120896, https://doi.org/10.1016/j.biomaterials.2021.120896.

[29] B. Chertok, R. Langer, Circulating magnetic microbubbles for localized real-time control of drug delivery by ultrasonography-guided magnetic targeting and ultrasound, Theranostics 8 (2018) 341–357, https://doi.org/10.7150/thno.20781.

[30] E. Beguin, et al., Magnetic microbubble mediated chemo-sonodynamic therapy using a combined magnetic-acoustic device, J. Control. Release 317 (2020) 23–33, https://doi.org/10.1016/j.jconrel.2019.11.013.

[31] E.S. Prikhozhdenko, et al., Target delivery of drug carriers in mice kidney glomeruli via renal artery. Balance between efficiency and safety, J. Control Release 329 (2021) 175–190, https://doi.org/10.1016/j.jconrel.2020.11.051.

[32] R.A. Barmin, et al., Air-filled bubbles stabilized by gold nanoparticle/photodynamic dye hybrid structures for theranostics, Nanomaterials 11 (2021) 415, https://doi.org/10.3390/nano11020415.

[33] D. Nečas, P. Klapetek, Gwyddion: an open-source software for SPM data analysis, Centr. Eur. J. Phys. 10 (2012) 181–188, https://doi.org/10.2478/s11534-011-0096-2.

[34] E.S. Vavaev, et al., CaCO3 nanoparticles coated with alternating layers of poly-L-arginine hydrochloride and Fe3O4 nanoparticles as navigable drug carriers and hyperthermia agents, ACS Appl. Nano Mater. 5 (2022) 2994–3006, https://doi.org/10.1021/acsanm.2c00338.

[35] E.V. Lyubin, M.D. Khokhlova, M.N. Skryabina, A.A. Fedyanin, Cellular viscoelasticity probed by active rheology in optical tweezers, J. Biomed. Opt. 17 (2012) 101510, https://doi.org/10.1117/1.JBO.17.10.101510.

[36] M.N. Romodina, M.D. Khokhlova, E.V. Lyubin, A.A. Fedyanin, Direct measurements of magnetic interaction-induced cross-correlations of two microparticles in Brownian motion, Sci. Rep. 5 (2015) 10491, https://doi.org/10.1038/srep10491.

[37] I.V. Vidiasheva, et al., Transfer of cells with uptaken nanocomposite, magnetite-nanoparticle functionalized capsules with electromagnetic tweezers, Biomater. Sci. 6 (2219–2229) (2018) 2219–2229, https://doi.org/10.1039/C8BM00479J.

[38] M.A. Kurochkin, I.V. Fedosov, D.E. Postnov, Toward label-free imaging of brain vasculature: frame-by-frame spatial adaptive filtration and adaptive PIV approaches, Eur. Phys. J. Plus 136 (2021) 719, https://doi.org/10.1140/epjp/s13360-021-01700-9.

[39] R.A. Barmin, et al., Impact of fluorescent dyes on the physicochemical parameters of microbubbles stabilized by albumin-dye complex, Colloids Surf. Physicochem. Eng. Asp. 647 (2022) 129095, https://doi.org/10.1016/j.colsurfa.2022.129095.

[40] A. Barik, K.I. Priyadarsini, H. Mohan, Photophysical studies on binding of curcumin to bovine serum albumin, Photochem. Photobiol. 77 (2003) 597–603, https://doi.org/10.1562/0031-8655(2003)0770597PSOBOC2.0.CO2.

[41] V. Boeris, B. Farruggia, G. Picó, Chitosan-bovine serum albumin complex formation: a model to design an enzyme isolation method by polyelectrolyte precipitation, J. Chromatogr. B Anal. Technol. Biomed. Life Sci. 878 (2010) 1543–1548, https://doi.org/10.1016/j.jchromb.2010.04.008.

[42] R.A. Barmin, et al., Albumin microbubbles conjugated with zinc and aluminum phthalocyanine dyes for enhanced photodynamic activity, Colloids Surf. B: Biointerfaces 219 (2022) 112856, https://doi.org/10.1016/j.colsurfb.2022.112856.

[43] S. Bhattacharjee, DLS and zeta potential - what they are and what they are not? J. Control. Release 235 (2016) 337–351, https://doi.org/10.1016/j.jconrel.2016.06.017.

[44] E.M. Brown, C. Katz, R. Butters, O. Kifor, Polyarginine, polylysine, and protamine mimic the effects of high extracellular calcium concentrations on dispersed bovine parathyroid cells, J. Bone Miner. Res. 6 (1991) 1217–1226, https://doi.org/10.1002/jbmr.5650061112.

[45] B. Glancy, R.S. Balaban, Role of mitochondrial Ca2+ in the regulation of cellular energetics, Biochemistry 51 (2012) 29592973, https://doi.org/10.1021/bi2018909.

[46] A.H. Khan, et al., Effectiveness of oil-layered albumin microbubbles produced using microfluidic T-junctions in series for in vitro inhibition of tumor cells, Langmuir 36 (2020) 11429–11441, https://doi.org/10.1021/acs.langmuir.0c01557.

[47] Deng, Q. *et al.* Superiorly stable three-layer air microbubbles generated by versatile ethanol–water exchange for contrast-enhanced ultrasound theranostics. ACS Nano 17, 263–274 (2023). doi:https://doi.org/10.1021/acsnano.2c07300.

[48] C.-J. Yu, S.-M. Wu, W.-L. Tseng, Magnetite nanoparticle-induced fluorescence quenching of adenosine triphosphate–BODIPY conjugates: application to adenosine triphosphate and pyrophosphate sensing, Anal. Chem. 85 (2013) 8559–8565, https://doi.org/10.1021/ac400919j.

[49] M.V. Novoselova, et al., Focused ultrasound-mediated fluorescence of composite microcapsules loaded with magnetite nanoparticles: in vitro and in vivo study, Colloids Surf. B: Biointerfaces 181 (2019) 680–687, https://doi.org/10.1016/j.colsurfb.2019.06.025.

[50] Lentacker, I., Geers, B., Demeester, J., Smedt, S. C. De & Sanders, N. N. Design and evaluation of doxorubicin-containing microbubbles for ultrasound-triggered doxorubicin delivery: cytotoxicity and mechanisms involved. Mol. Ther. 18, 101–108 (2010). doi:https://doi.org/10.1038/mt.2009.160.

[51] S. Tinkov, G. Winter, C. Coester, New doxorubicin-loaded phospholipid microbubbles for targeted tumor therapy: part I — formulation development and in-vitro characterization, J. Control. Release 143 (2010) 143–150, https://doi.org/10.1016/j.jconrel.2009.12.026.

[52] J. Zhang, et al., Protein–polymer nanoparticles for nonviral gene delivery, Biomacromolecules 12 (2011) 1006–1014, https://doi.org/10.1021/bm101354a.

[53] P. Shi, et al., Elastin-based protein polymer nanoparticles carrying drug at both corona and core suppress tumor growth in vivo, J. Control. Release 171 (2013) 330–338, https://doi.org/10.1016/j.jconrel.2013.05.013.

[54] S.A. Ghadami, Z. Ahmadi, Z. Moosavi-Nejad, The albumin-based nanoparticle formation in relation to protein aggregation, Spectrochim. Acta Part A Mol. Biomol. Spectrosc. 252 (2021) 119489, https://doi.org/10.1016/j.saa.2021.119489.

[55] I.L. Zhuravleva, E.A. Bezrodnykh, B.B. Berezin, V.E. Tikhonov, Y.A. Antonov, Effect of soft preheating of bovine serum albumin on the complexation with oligochitosan: structure and conformation of BSA in the complex, Macromol. Biosci. 23 (2023) 2300088, https://doi.org/10.1002/mabi.202300088.

[56] Helbert, A. *et al.* Monodisperse versus polydisperse ultrasound contrast agents: in vivo sensitivity and safety in rat and pig. Ultrasound Med. Biol. 46, 3339–3352 (2020). doi:https://doi.org/10.1016/j.ultrasmedbio.2020.07.031.

[57] J.A. Navarro-Becerra, J.I. Castillo, F. Di Ruzza, M.A. Borden, Monodispersity increases adhesion efficiency and specificity for ultrasound-targeted microbubbles, ACS Biomater. Sci. Eng. 9 (2023) 991–1001, https://doi.org/10.1021/acsbiomaterials.2c00528.

[58] F. Domenici, et al., Long-term physical evolution of an elastomeric ultrasound contrast microbubble, J. Colloid Interface Sci. 540 (2019) 185–196, https://doi.org/10.1016/j.jcis.2018.12.110.

[59] M.V. Novoselova, et al., Polymer/magnetite carriers functionalized by HER2-DARPin: avoiding lysosomes during internalization and controlled toxicity of

doxorubicin by focused ultrasound induced release, Nanomedicine 47 (2023) 102612, https://doi.org/10.1016/j.nano.2022.102612.
[60] S. Piao, R.K. Amaravadi, Targeting the lysosome in cancer, Ann. N. Y. Acad. Sci. 1371 (2015) 45–54, https://doi.org/10.1111/nyas.12953.
[61] K. Yanagisawa, F. Moriyasu, T. Miyahara, M. Yuki, H. Iijima, Phagocytosis of ultrasound contrast agent microbubbles by Kupffer cells, Ultrasound Med. Biol. 33 (2007) 318–325, https://doi.org/10.1016/j.ultrasmedbio.2006.08.008.
[62] M. Liu, et al., Strategies to maximize anthracycline drug loading in albumin microbubbles, ACS Biomater. Sci. Eng. (2021), https://doi.org/10.1021/acsbiomaterials.1c01203.
[63] O.A. Mayorova, O.I. Gusliakova, E.S. Prikhozhdenko, R.A. Verkhovskii, D. N. Bratashov, Magnetic platelets as a platform for drug delivery and cell trapping, Pharmaceutics 15 (2023) 214, https://doi.org/10.3390/pharmaceutics15010214.
[64] P. Menna, O.G. Paz, M. Chello, E. Covino, Anthracycline cardiotoxicity, Expert Opin. Drug Saf. 11 (sup1) (2012) S21–S36, https://doi.org/10.1517/14740338.2011.589834.
[65] P.A. Henriksen, Anthracycline cardiotoxicity: an update on mechanisms, monitoring and prevention, Heart 104 (2018) 971–977, https://doi.org/10.1136/heartjnl-2017-312103.